Attached please find copies of publications that resulted from the work supported by DE-SC0005318.

ResearchGate

See discussions, stats, and author profiles for this publication at: https://www.researchgate.net/publication/264312434

Effect of Dielectric Properties of Ceramic-Solvent Interface on the Binding of Protein to Oxide Ceramics: a Non Local Electrostatic Approach

Article · July 2014

Source: arXiv

READS

22

3 authors, including:



Alexander Rubinstein

Ariel University

18 PUBLICATIONS **133** CITATIONS

SEE PROFILE



Fereydoon Namavar

University of Nebraska Medical Center

254 PUBLICATIONS **2,386** CITATIONS

SEE PROFILE

All in-text references underlined in blue are linked to publications on ResearchGate, letting you access and read them immediately.

Available from: Fereydoon Namavar
Retrieved on: 19 August 2016

Effect of Dielectric Properties of Ceramic-Solvent Interface on the Binding of Protein to Oxide Ceramics: a Non Local Electrostatic Approach

A.I. Rubinstein[1*], R. F. Sabirianov[2*], F. Namavar[1]

[1]Department of Orthopaedic Surgery and Rehabilitation, University of Nebraska Medical Center, Omaha, NE 68198; [2]Department of Physics, University of Nebraska at Omaha, Omaha, NE 68182

Abstract

The contribution of electrostatic interactions to the free energy of binding between model protein and a ceramic implant surface in the aqueous solvent, considered in the framework of the non-local electrostatic model, is calculated as a function of the implant low-frequency dielectric constant. We show that the existence of a dynamically ordered (low-dielectric) interfacial solvent layer at the protein-solvent and ceramic-solvent interface markedly increases charging energy of the protein and ceramic implant, and consequently makes the electrostatic contribution to the protein-ceramic binding energy more favorable (attractive). Our analysis shows that the corresponding electrostatic energy between protein and oxide ceramics depends non-monotonically on the dielectric constant of ceramic, ε_C. Obtained results indicate that protein can attract electrostatically to the surface if ceramic material has a moderate ε_C below or about 35 (in particularly ZrO_2 or Ta_2O_5). This is in contrast to classical (local) consideration of the solvent, which demonstrates an unfavorable electrostatic interaction of protein with typical metal oxide ceramic materials (ε_C>10). Thus, a solid implant coated by combining oxide ceramic with a reduced dielectric constant can be beneficial to strengthen the electrostatic binding of the protein-implant complex.

Keywords: non-local electrostatics, solvent permittivity, interfacial water, ceramic implants, protein adsorption, biocompatibility.

Introduction

The response of biological cells to artificial implant surfaces critically depends on their morphology (at the nano–scale), charge distribution, and physicochemical properties that strongly affect the molecular and macromolecular interactions that take place at the implant interface[1,2,3]. Because cells can adhere and function on the implant surface with the help of the extracellular matrix (ECM) proteins,[4,5] understanding mechanisms of the adhesive protein adsorption or formation of the protein-implant surface complexes on the nano-scale level is the key objective in the interdisciplinary study of the biocompatibility and bio-integration of implanted devices. Despite the importance of the above problem, the analysis of the protein adsorption on inorganic surfaces remains a challenge[6,7,8]. One of the very important components of the adsorption energy is attractive electrostatic interactions (EI) between a protein and the surface. Nevertheless its estimation is rather poorly studied due to the absence an adequate consideration of the dielectric response at the protein-solvent and implant-solvent interfaces that determine EI in the protein-solvent-implant interfacial system at the distances comparable with the dynamic solvent microstructure[6,9]. Thus, an accurate description of EI between the protein and solid implant in the aqueous solvent during the adsorption process is needed.

When a dielectric implant surface has effective distributed charges the protein-implant association should be governed mainly by EI prior to establishing substantial surface contacts. There is a competition between contribution of the long-range favorable (attractive) EI and the unfavorable contribution due to electrostatic desolvation of both protein and implant to the association binding energy. The latter contribution is a result of an exclusion of the high-dielectric aqueous solvent when a low-dielectric protein approaches the implant surface (glasses, polymers, ceramics, and other). Thus, the displacement of water molecules from implant surface presents a substantial energy barrier to protein adsorption[10,11]. As a consequence, contribution of EI to the binding energy should be significantly large to compensate or exceed the desolvation effect to facilitate the formation of the protein-implant complex. At the same time, in traditional classic (CL) consideration of the aqueous solvent, the electrostatic contribution to the protein adsorption energy is not significant even so due to the strong electrostatic screening by the aqueous solvent with a high dielectric constant (~80). Thus, a substantial electrostatic binding protein and solid implant is far from evidence. However, several studies[8,12,13,14] (see also Ref.1 and references cited therein) show that protein adsorption does occur on surfaces of hydrophilic materials, where EI provide the necessary driving force for protein adsorption.

Variety of implant materials are commonly used in clinical medicine. Among them gold, carbon and related materials are conducting, while many of biocompatible implants made of dielectric materials such as polyethylene and oxide ceramics including zirconia, titania and tantalum oxide due to their excellent biocompatibility. Typically, the surface of widely used metallic implants such as titanium is oxidized. It has been shown that a titanium surface oxidizes (forms predominantly as dioxide in rutile structure) has the depth of oxidation up to about 8 nm[15,16]. Modifying the surface oxide layers by coating them with ceramics such as zirconia and titania may further improve the properties of implant materials. Particularly, nanostructuring the coating of orthopedic implants can drastically affect their mechanical, dielectric, and wetting properties[17]. Oxide ceramics may be prepared to have similar surface topology and, therefore, this allows comparative experimental studies of protein-surface interaction by addressing the effect of selected property, e.g. dielectric constant, varying in these materials.

The implant dielectric constant, ε_C, of the above dielectrics can vary in range from about 2 in polyethylene to above 300 for $SrTiO_3$. This constant can be selectively tuned in some oxide ceramics to modify the dielectric properties of the surface oxide layer (e.g. TiO_2). Titania-based ceramics may have a dielectric constant anywhere between 25 and 114[18]. It is known that surface defects of solid state insulators such as vacancies, steps and edges may have charged states[19]. The interactions between these effective charges and the charged patches of protein depend on the dielectric nature of the implants. It is important to reveal such solid implants that provide the best conditions for forming electrostatically induced protein-implant association.

Experimentally, the amount of protein adsorbed on the surface can be evaluated by ELISA (enzyme-linked immunosorbent assay)[24], fluorescent labeling in PSIM (protein-surface interaction microarrays)[20], radiolabeling or related methods. These methods provide quantitative measure of protein binding affinity to the surface as function of solvent pH or surface parameters (such as roughness). However, these methods do not provide direct information on the binding strength of macromolecules to the surface. In combination with Raman spectroscopy (or Surface Enhanced Raman Spectroscopy) a fingerprints of specific bonding can be identified. Force spectroscopy (based on AFM) was used to measure, in aqueous environment, the dispersion force due to the polymer adsorbed on the substrate. The latter was applied to analysis of protein adsorption on charged surfaces. For example, Meadows et al. (and referenced therein) show that

the loading-rate plots contains only a single rupture, which most likely probe a specific surface-protein (fibronectin) interaction[21]. This allows finding the value of the free energy for macromolecule dissociation from the surface. This method allows, in principle, measuring the trends of macromolecule-surface interaction depending on surface parameters (such as charge, preparation conditions, or dielectric constant).

Both experimental studies[22,23] and results of simulations[24,25] show that not only immobilization but also activation (partial unfolding) of the adhesive proteins (such as fibronectin) is affected by negative charges on silica, mica, and other hydrophilic (oxide) surfaces as well as onto the nano-structured surface. These electrostatically induced events should promote ECM formation[4,5,26] that governs cell adhesion and, as a result, cell functioning on the implant surface. Understanding protein activation associated with the general problem of protein partial unfolding, particularly at the inorganic surfaces, is one of the fundamental goals in modern computational bio-chemistry, biomedical sciences, and nanotechnology[1,27,28]. Although there is great research interest to the electrostatic component of the protein adsorption and activation at the inorganic surface, relevant EI estimations are still poor and frequently restricted to CL electrostatics models[1,3,29].

The electrostatic free energy (ΔG_{EI}) of binding between protein and implant can be calculated as corresponding energy for two interacting macromolecules, in particular protein P and ceramic particle C associated into the complex CP. This energy in an aqueous solvent can be computed (analogously to a protein-protein complex) as the difference in the electrostatic free energy between bound (ΔG^{CP}) and unbound protein (ΔG^{P}) and ceramic particle (ΔG^{C}) states[30]:

$$\Delta G_{EI} = \Delta G^{CP} - (\Delta G^{C} + \Delta G^{P}) = \frac{1}{2}\left[\sum_{i\in(C,P)} (q_i\Phi_i)^{CP} - \sum_{i\in C} (q_i\Phi_i)^{C} - \sum_{i\in P} (q_i\Phi_i)^{P} \right], \qquad (1)$$

where the summation is over all the charges q_i located in the macromolecule(s), and Φ_i is the electrostatic potential at the position of q_i. The electrostatic potential can be calculated using the Poisson-Boltzmann equation in the framework of CL electrostatics with a local relation between the field and its electric induction [30 ,31,32]. Commonly, this approach is treating the interfacial solvent water as bulk, i.e. assuming that its dielectric constant to be ~ 80. However, there is growing number of experimental[33,34] and theoretical[35,36] studies pointing to the existence of a partially structured interfacial water layer with dielectric properties distinct from the bulk solvent. Due to the low rotational mobility of water dipole molecules of the solvent at a dielectric-solvent interface (where dielectric is a protein-like or ceramic medium), the effective dielectric permittivity of the layer is significantly reduced[37,38,39]. Thus, it is necessary to develop more adequate approaches for EI evaluations that can accurately take the above spatial heterogeneity of the solvent into account. Recently, a continuum non-local (NL) electrostatic model, adopting an integral relationship between the electric field and its induction, was developed to analyze the effects of the spatial heterogeneity of the effective dielectric properties at the protein-solvent interface [9, .3232, 40.]. Particularly, it was shown that the presence of an extended dynamically ordered water shell at the dielectric-solvent interface with substantially reduced effective dielectric permittivity resulted in the prominent decline of the electric field screening in the vicinity of the interface. This model explains the high magnitude of the protein association rate constants in the protein kinetics [40]. Recently, we have shown that the electrostatic contribution of the protein binding free energy is much stronger (in comparison with CL consideration) due to the existence of the low-dielectric interfacial water shell on the surface of

the protein-like dielectric media[9]. This effect can be a major factor capable of compensation for the desolvation effect in the formation of the protein complex. A similar statement can be made about the protein-implant binding free energy during the initial protein adsorption on the inorganic (ceramic implant) surfaces.

In our study, to assess the role of the electrostatic contribution to the binding free energy of protein-ceramic association, ΔG_{EI}, we considered a simple system that is composed of two model macromolecules (represented by continuous medium), in particular, protein P and ceramic C. Single point charges of opposite signs are located at their respective surfaces in the region of functional patches (binding sites). The bound state of the protein-ceramic complex, CP, assumes the contact of these particles at the location of opposite charges by their binding sites. To estimate the electrostatic free energy of the point charge placed into the isolated particle (P and C) in close proximity to the solvent interface (ΔG^P, ΔG^C), we calculated the corresponding "charge image potential" (IP) acting on the above charge due to its electrostatic interaction with the induced polarization at the interface[9]. We used the concept of the NL electrostatics and phenomenological theory of polar solvent[32,40] (and references cited therein). Assuming that the charges located at the particle binding sites are in close proximity to their molecular surface, the interface in the vicinity of the charge was approximated as a locally flat (planar) solvated region.

Here, we analyze the electrostatic free energy ΔG_{EI} of the model protein-ceramic binding for NL and CL solvent consideration as a function of the ceramic dielectric constant ε_C. Our calculations shows that taking into account the NL electrostatic effect of the solvent (the low-dielectric interfacial water shell on the dielectric interface) significantly shifts (to the negative values) the electrostatic contribution to the binding free energy of the protein-ceramic association, ΔG_{EI}, compared to the CL solvent model. This results in the strong favorable electrostatic contribution to the protein-ceramic complex formation for a wide range of ceramic materials. In particular, ΔG_{EI} calculated for the protein complex on the ZrO_2 surface is more favorable than for other ceramic surfaces including known biocompatible materials such as Ta_2O_5 and TiO_2.

METHODS

We analyzed the electrostatic interactions at the model dielectric-solvent interface using NL electrostatic approach[9, 32., 40]. In this approach, the linear dielectric response for each of the media in contact is presented by the integral non-local relation between the electric induction **D** and the electric field **E**:

$$D_{m,\alpha}(\mathbf{r}) = \sum_{\beta} \int_{Vm} \varepsilon_{m,\alpha\beta}(\mathbf{r},\mathbf{r'})\, E_{m,\beta}(\mathbf{r'})\, d\mathbf{r'}, \qquad \alpha, \beta = x, y, z \tag{2}$$

where m = 1, 2 refers to the media, solvent, and solute; the function $\varepsilon_{m,\alpha\beta}(\mathbf{r}, \mathbf{r'})$ is the dielectric permittivity tensor that is determined by the spatial correlation induced by the polarization of the medium; and the integration is taken over the volume V_m of the medium. The main purpose of this approach is to incorporate the short-range structure of the contacting media into electrostatics.

We used the planar dielectric boundary to model the interface between dielectric (ceramic) including a protein-like medium (dielectric solute) and solvent (i.e. both media are semi-infinite). Integrations were performed using a cylindrical coordinate system, (R, Z), as

shown in Figure 1, where Z is the axis perpendicular to the plane passing through the boundary, and R is the radius vector in this plane. The semi-infinite regions $Z < 0$ and $Z > 0$ were assigned to a solvent and a solute, respectively. The charge $Q = \xi e$ (ξ is the fraction of the electron charge e) is located in the solute at point $(0, Z_0)$.

In the framework of the so-called "specular reflection approximation" model for the system of two semi-infinite media [32, 54] which we adopted here, the properties of the media along the plane of the boundary are considered as homogeneous isotropic with $\varepsilon_{m,\alpha\beta}(\mathbf{r}, \mathbf{r'}) = \varepsilon_{m,\alpha\beta}(Z, Z', \mathbf{R-R'})$ and can be expressed through the bulk dielectric function[41]. The differential form of Gauss's law[42] was applied with non-local relationship Eq.(2) in order to compute the electrostatic potential φ (R, Z, Z_0) created by charge Q in any point (R, Z) with $Z > 0$. The potential is expressed in terms of the Fourier-transformed dielectric functions $\varepsilon_1(\mathbf{r-r'})$ and $\varepsilon_2(\mathbf{r-r'})$ ($\varepsilon_1(k)$ and $\varepsilon_2(k)$, respectively), which characterize the bulk dielectric properties of the solvent and solute, respectively[9,32, 54].

The corresponding image potential IP, $W(Z_0)$, is defined as a change in free energy of the system when transferring charge Q from infinity (bulk of the solute) to the point R=0, $Z=Z_0$ at the interface. It was calculated using Fourier-Bessel transformation in the Güntelberg charging cycle approach[43, 54]:

$$W(Z_0) = \frac{Q}{4\pi} \lim_{z \to z_0} \int_0^{+\infty} dK K\left[\varphi(K,Z,Z_0) - \varphi^0(K,Z,Z_0 \to \infty)\right], \qquad (3)$$

where φ^0 (K, Z, $Z_0 \to \infty$) denotes the electrostatic potential when the charge is located at infinity. In order to analyze the behavior of the IP potential for ceramics and protein, the dielectric solute was considered as a uniform dielectric medium with the dielectric constant $\varepsilon_2(k) = \varepsilon_C$. In the case of proteins, $\varepsilon_2(k) = \varepsilon_p = 4$[44]. For several typical ceramics, ε_C is determined as a specific dielectric (low-frequency mode) constant: polyethylene, $\varepsilon_C = 2$; SiO_2, $\varepsilon_C = 3.9$[45]; quartz,$\varepsilon_C = 4.43$; ε_C of Ta_2O_5 is in the range of 20-52[46,47,48]; ε_C of zirconia in monoclinic phase is ~20-28[49], and similar values for its cubic phase stabilized by yttria[50]. The rutile phase of TiO_2 (also a phase of native surface oxide layer) has ε_C~114[51,52,53]. The static dielectric permittivity of TiO_2 anatase phase was originally reported to be ~31[51].. Fukushima and Yamada have shown that the dielectric constant of anatase TiO_2 may vary between 35 and 108 depending on preparation conditions[18].

The dielectric function ε_1 (k) in the bulk of the aqueous solvent was approximated in the context of polar solvent phenomenological model [32, 40, 54]:

$$\varepsilon_1(k) = \varepsilon^* + (\varepsilon_s - \varepsilon^*)/[1 + (Lk)^2 \varepsilon_s / \varepsilon^*], \qquad (4)$$

where $\varepsilon^* = 6$ and $\varepsilon_s = 78.3$ are short- and long-wavelength dielectric constants of the solvent at room temperature; and L is the correlation length of the water dipoles, which is proportional to the characteristic length of the hydrogen-bonding network of water molecules (~3-5Å). The dielectric function ε_1 (k) is the "one pole approximation" which effectively separates the spectrum of the polarization fluctuations of water into two parts: (i) the low-frequency zone associated with the orientational Debye mode; and (ii) the high-frequency zone associated with infrared and optical modes. This approximation takes into account the orientational Debye polarization and neglects the higher frequency modes[32, 55,56,57].The polarization modes within the orientational mode are correlated in space with effective correlation radius L (due to the strong non-electrostatic interactions), while the polarization modes with the high-frequency are

assumed to be uncorrelated [55, 58]. The dielectric constant, determined within the transparency zone of the electromagnetic absorption (which separates frequencies typical for low- and high-frequency zones), corresponds to the short-wavelength dielectric constant ε_* [55, 58]. Thus, the "one pole approximation" dielectric model for water assumes that the function ε_1 (k) is changed at the length-scale ~ L from the values characteristic for the macroscopic, long-wavelength dielectric constant, ε_s, to the value of the short-wavelength dielectric constant $\varepsilon_* \cong 6$ [55, 56, 58]. The "one pole approximation" was found to be adequate for the description of polar molecules without internal degrees of freedom, such as rigid, strongly correlated dipoles[55].

Quantities ε_* and L of water can be adjusted/selected by fitting to the experimental data analyzed in terms of the free energy of interaction between protonated amino groups in dibasic amines [57]. Function $\varepsilon_1(k)$ in Eq.(4) was applied in the framework of the NL electrostatic approach to explain several experimental data in the electrolyte theory, interfacial electrochemistry, and computational biophysics[9, 32, 40] (and references cited therein).

The electrostatic free energy of the dielectric solute (ceramic and protein) in the unbound states ΔG^C and ΔG^P was calculated using Eq.(3). $W(Z_0)$ potential in the k_BT energy units can be written in the form of[9]

$$W(Z_0)/(560\, k_BT\, \xi^2) = (4\varepsilon_d Z_0)^{-1} \int_0^{+\infty} dx\, S(x, \eta)\, \exp(-x), \qquad (5)$$

$$S(x, \eta) = [D(x, \eta) - 1/\varepsilon_d\,]/\,[D(x, \eta) + 1/\varepsilon_d\,],$$

$$D(x, \eta) = (1/\varepsilon_S) + (1/\varepsilon_* - 1/\varepsilon_S)\,[1 + (x\eta)^{-2}]^{-1/2},$$

where $\eta = L/2Z_0$ is a dimensionless parameter, ε_d is solute dielectric constant and $Q^2 = \xi^2 e^2 = 560\, k_BT\, \xi^2$.

The results of the asymptotic and numerical analysis of the above IP potential [9] and pair wise electrostatic interaction energy at the interface [32,40] suggest that a layer of interfacial water on the solute dielectric surface has effective (i.e. distance- dependant) dielectric properties different from the bulk solvent . The corresponding effective dielectric permittivity of the above interfacial solvent layer was calculated as a function of distance from the interface[9, 40]. The magnitude of the function is ~ $(\varepsilon_d + \varepsilon_*)/2$ at small $Z \sim Z_0 < L$ (in close proximity to the interface), while it approaches ~$(\varepsilon_d + \varepsilon_S)/2$ at the large distances $Z \sim Z_0 > 10$-15 Å. The validity of these average dielectric constants at the interface is also supported by recent work[59]. It should be noted that the occurrence of a low-dielectric layer on the dielectric surface is consistent with the experimental study of hydration dynamics on the protein surface [34, 40] (and references cited therein).

RESULTS AND DISCUSSION

The electrostatic binding energy between protein and ceramic (two solutes), forming the complex, was calculated using the above model of idealized (planar) interface of proteins P and ceramic C. The protein possesses a single ion charge (for example $+e$) located at the protein surface interacting patches or protein "binding site". Analogously, the ceramic also possesses a single electron charge of opposite sign ($-e$) located at the ceramic surface interacting patch ($\xi_P = \xi_C = 1$). Both charges were considered as a point charge located in the solute (P and C media) in the proximity of interface. The bound state of the CP complex occurs through the contact of

the corresponding binding sites (facing each other) of protein P and ceramic C. The point charges of the binding sites in the bound pair are assumed to have a minimal inter-charge distance of r_{12}. This distance is about $r_{12}= 2r_{ion} \approx 5$ Å, where $r_{ion} \approx 2.5$ Å is the closest proximity of a charged center of an ionogenic group of amino acid residue to the molecular protein surface. The size of the adhesive protein is usually much larger than ionic radius, thus, justifying the planar interface approximation in the vicinity of the charge to estimate the electrostatic component of the free energy of binding in the bound state. However, when the size of protein is comparable to the ionic radius, the curvature of the interface cannot be neglected and corresponding correction needs to be included[60,61]. The similar planar approximation can be used for the smooth ceramic surfaces when the local curvatures of its surface features are small compared with inverse inter-atomic distances in the ceramic (~2-3Å).

The electrostatic free energy of the bound system in planar interface approximation is described by the first term of Eq.(1). This is a Coulomb interaction energy at the interface of the CP complex between the protein and ceramic with dielectric constant ε_P and ε_C, respectively, and the inter-charge distance of r_{12} mentioned above [42]:

$$\Delta G^{CP}/(560\ \xi_P\xi_C k_B T) = -1/(\varepsilon_{eff} r_{12}), \qquad (6)$$
$$\varepsilon_{eff} = (\varepsilon_P + \varepsilon_C)/2,$$

where $k_B T \approx 0.593$ kcal/mol at 25°C.

We calculated the electrostatic energy of the unbound states ΔG^C and ΔG^P as the IP potential, Eq.(3). All calculations were performed with a typical distance Z_0=2.5Å. The behavior of the ΔG^C for the charge located in the dielectric media (ceramic) as a function of the media dielectric constant ε_C considered in NL ($\varepsilon_* = 6$, $\varepsilon_S = 78.3$, L = 5 Å) and CL ($\varepsilon_S = \varepsilon_* = 78.3$) solvent approximation is shown in Figure 2. As we can see in Figure 2, the results of numerical calculations obtained for Eq.(5) are consistent with result of our asymptotic analysis carried out in the CL case [42]:

$$\frac{\Delta G^C_{CL}(\varepsilon_C, Z_0)}{560\xi^2 k_B T} = \frac{1}{4Z_0\varepsilon_C}\frac{\varepsilon_C - \varepsilon_S}{\varepsilon_C + \varepsilon_S}, \quad Z_0 > 0,$$

and NL consideration[9]

$$\frac{\Delta G^C{}_{NL}(\varepsilon_C, Z_0)}{560\xi^2 k_B T} = \frac{1}{4Z_0\varepsilon_C}\frac{\varepsilon_C - \varepsilon_*}{\varepsilon_C + \varepsilon_*}, \quad Z_0 << L.$$

The asymptotic and numerical analyses of the ΔG^C indicate this energy is negative (attractive interactions) at the small values of the ceramic dielectric constant ($\varepsilon_C < \varepsilon_*, \varepsilon_S$), while ΔG^C has a positive value (repulsive interactions) at the large values ($\varepsilon_C > \varepsilon^*, \varepsilon_S$) both in CL and NL consideration (Figure 2). The previously found significant decrease of dielectric permittivity of the solvent at the interface is responsible for this effect[9]. The corresponding value of ΔG^P for the charge located in the protein (ε_P=4, Z_0=2.5Å) was calculated as ΔG^P=-12.6k_BT for CL and ΔG^P =-6.6k_BT for NL solvent consideration[9].

The electrostatic free energies $\Delta G_{NL,EI}$ and $\Delta G_{CL,EI}$ of the model protein-ceramic binding accordingly for NL and CL solvent consideration were calculated as a function of the ceramic

dielectric constant ε_C using Eq.(1), where ΔG^{CP} is calculated by Eq.(6), and ΔG^C and ΔG^P - by Eq.(5) with $\varepsilon_d=\varepsilon_C$ and $\varepsilon_d=\varepsilon_p=4$, respectively. The numerical calculation of the ΔG_{EI}, ΔG^{CP}, and ΔG^C energies for several typical dielectrics are summarized in Tables 1 and 2 for the NL and CL approximation, respectively. Figure 3 shows the electrostatic contribution to the binding free energy of protein-ceramic association ($\Delta G_{NL,EI}$) is shifted significantly (to the negative values)

Table 1. The numerical calculation of the ΔG^C, ΔG^{CP} and ΔG_{EI} energies for several typical dielectrics in the case of the non-local (NL) electrostatic model of the solvent

Dielectric materials	Dielectric constant, ε_C	ΔG^C [k_BT]	ΔG^{CP} [k_BT]	$\Delta G_{NL,EI}$ [k_BT]
Polyethylene	2	-19.29	-37.33	-11.42
Quartz	4	-6.62	-28.00	-14.76
ZrO2	25	0.71	-7.72	-1.81
Ta2O5	30	0.73	-6.59	-0.70
TiO2	110	0.39	-1.96	+4.27

Table 2. The numerical calculation of the ΔG^C, ΔG^{CP} and ΔG_{EI} energies for several typical dielectrics in the case of the classical (CL) electrostatic model of the solvent

Dielectric materials	Dielectric constant, ε_C	ΔG^C [k_BT]	ΔG^{CP} [k_BT]	$\Delta G_{CL,EI}$ [k_BT]
Polyethylene	2	-26.60	-37.33	1.9
Quartz	4	-12.63	-28.00	-2.74
ZrO2	25	-1.16	-7.72	+6.07
Ta2O5	30	-0.83	-6.59	+6.87
TiO2	110	0.085	-1.96	+10.59

when we apply NL electrostatic solvent model compared to the CL one. As it follows from obtained results (Figure 3), the electrostatic free energy of the protein–surface complex calculated using CL consideration of the aqueous solvent is unfavorable for most of metal oxide ceramics. At the same time, consideration of the solvent by the NL electrostatic model reveals significant strengthening of the electrostatic contribution to the binding energy making the protein-surface complex formations electrostatically favorable for dielectric constant $\varepsilon_C<35$. In this case, the complex formation remains unfavorable for ε_C over 35, but ΔG_{EI} is considerably reduced. Origin of the above effect reflects the significant increase of ΔG^C and ΔG^P energies due to presence of a low-dielectric solvent layer on the ceramic and protein surface in the process of the protein-ceramic association in the solvent (see Tables 1 and 2). It should emphasize that ΔG^P is a negative value and provides the same significant shift for ΔG_{EI} at all ε_C values. The energy ΔG_{EL} is a non-monotonic function of ε_C, and ΔG_{EL} increases smoothly as a function of ε_C in both CL and NL solvent consideration from minimum at $\varepsilon_C=4$. This is because the pairewise Coulomb interaction energy at the interface ΔG^{CP}, Eq.(6), is negative and inversely proportional to $(\varepsilon_P+\varepsilon_C)$, while ΔG^C, Eq.(5), is positive at large ε_C (as it is following from Figure 2 and asymptotic analysis). At the small ε_C, ΔG^C becomes negative (Figure 2) and increases rapidly in

magnitude when ε_C decreases. As a result, ΔG_{EI} becomes positive (repulsive) at very small ε_C (Figure 3).

The ceramics with dielectric constants below a specific value (in our estimations ~35) favor the association of protein and surface into a complex due to the binding energy ΔG_{EI} (calculated by the NL solvent model) becomes negative in comparison with CL consideration (Figure 3). Thus, ΔG_{EI} calculated for a protein complex with the ZrO_2 surface is more favorable than for ceramic surfaces with larger dielectric constants (e.g. TiO_2: Tables 1). In fact, the low-dielectric boundary water layer on the protein and ceramic surface is responsible for favorable protein-ceramic complex formation ($\Delta G_{EI}<0$) for several ceramics indicated in Figure 3 by their respective typical low-frequency dielectric constants. Overall, our estimations show that the interfacial solvent layer with low dielectric permittivity on the both protein and ceramic surfaces is a major factor capable of compensation for the unfavorable desolvation effects in the protein adsorption on the dielectric implant surface.

It should be noted that the above consideration takes into account only a single oppositely-charged pair across the implant-protein interface. For this pair, for example in case of zirconia, (ΔG_{EI}) is ~ $-2k_BT$ (Table 1). At the same time, there are many oppositely-charged pairs at the protein-ceramic interface resulting in strong electrostatic attractive interaction. Thus, complimentary EI can be a driving force for protein adsorption and formation of protein-implant complexes. The formation of multiple charge patches on the ceramic surface can be achieved by surface modification such as patterning and/or nano-structuring. This is supported by studies showing that a sharper tantalum oxide curvature nanostructure promotes the adsorption and activation of adhesive protein such as fibronectin.[62]

The electrostatic binding between ceramic and adhesive protein can be strengthened by reducing the dielectric constant of the ceramic, and at the same time, increasing the concentration of surface-charged nanostructures. Based on our model calculations, we deduced that ZrO_2 or Ta_2O_5 coatings could have advantages with respect to TiO_2 or a native oxide on the surface of Ti, and provide stronger electrostatic binding. Furthermore, the co-alloying of these compounds with TiO_2 and reducing dielectric permittivity of the coating[18] can also strengthen the electrostatic component to the binding energy. Furthermore, nanostructuring of the TiO_2 coating promotes the formation of the anatase phase with a reduced dielectric constant (ε_C~30) may serve the same purpose. These results are in qualitative agreement with the studies of the fibronectin adsorption on various ceramic surfaces [62,63,64].

Conclusion

In the present work, we calculated and analyzed the contribution of electrostatic interactions (EI) to the free energy of binding between model protein and ceramic implant surface in the aqueous solvent as a function of the ceramic (solid implant) dielectric constant. We used non-local electrostatic approach[9, 32 ,40.] to take into account the solvent structure and the contribution of a solvent orientational polarization (correlated by the network of hydrogen bonds) into the pairwise EI at the considered interfaces with solvent.

We show that the existence of the low-dielectric boundary water layer at the protein-solvent ("dynamically ordered water") [32, .34.] interface and ceramic-solvent interface markedly strengthens the electrostatic contribution to the protein-ceramic binding energy (ΔG_{EI}) due to the increase of charging energy of the protein and ceramic implant (ΔG^C and ΔG^P energies) in aqueous solvent. Using the non-local electrostatic approach, we show the protein-implant

association is favorable (attractive) for implant dielectric constant $\varepsilon_C<35$, while consideration of the aqueous solvent as a uniform dielectric medium with high dielectric constant $\varepsilon_s = 78.3$ (that is typically assumed in classical local approach) predicts unfavorable (repulsive) EI between protein and a majority of typical metal oxide ceramic materials ($\varepsilon_C>10$).

The solid implants coated by oxide ceramics with reduced dielectric constants can be beneficial to strengthen the electrostatic binding of the adhesive proteins to the implant. In particular, we found that electrostatic binding energy for protein adsorption on the ZrO_2 or Ta_2O_5 surface is more favorable than for ceramic surfaces with a larger dielectric constant including known biocompatible materials such as TiO_2. Alternatively, metals such as Ta and Zr can improve implant biocompatibility, because their native oxide has lower dielectric constant. Such control of the protein adsorption at the surface is paving the way for development of a novel coating for orthopaedic implants.

Acknowledgement

The work at the University of Nebraska Medical Center in Omaha, NE, was supported by DOE grant, "Material Science Smart Coatings", Award No. DE-SC0005318. The work at the University of Nebraska at Omaha was supported by NSF-EPSCoR (Grant No. EPS-1010674), and DOE DE-EE0003174, and Nebraska Research Initiative.

References

(1) Gray, J. The interaction of proteins with solid surfaces. Curr. Opin. Struct. Biol. **2004**, 14, 110-115.

(2) Wilson, K.; Stuart, S.J.; Garcia, A.; Lator Jr., R.A. A molecular modeling study of the effect of surface chemistry on the adsorption of a fibronectin fragment spanning the 7-10th type III repeats. J. Biomed. Mater. Res. **2004,** 69A, 686.

(3) Makrodimitris, K.; Masica, D. L.; Kim, E. T.; Gray, J. J. Structure prediction of protein-solid surface interactions reveals a molecular recognition motif of statherin for hydroxyapatite. J. Am. Chem. Soc. **2007**, 129, 13713-13722.

(4) Allen, L.T.; Tosetto, M.; Miller, I.S.; O'Connor, D.P.; Penney, S.C.; Lynch, I.; Keenan, A.K.; Pennington, S.R.; Dawson, K.A.; Gallagher, W.M. Surface-induced changes in protein adsorption and implications for cellular phenotypic responses to surface interaction. Biomaterials **2006**, 27, 3096-3108.

(5) Cutler, S.M.; Garcia, A.J. Engineering cell adhesive surfaces that direct integrin alpha5beta1 binding using a recombinant fragment of fibronectin. Biomaterials **2003**, 24,1759-1770

(6) Kasemo, B. Biological surface science. Surface Science **2002**, 500, 656-677.

(7) Hook, F.; Kasemo, B.; Grunze, M.; Zauscher, S. Quantitative Biological Surface Science: Challenges and Recent Advances. NANO **2008**, 12, 2428-2436.

(8) Sabirianov, R.F.; Rubinstein. A.; Namavar, F. Enhanced initial protein adsorption on engineered nanostructured cubic zirconia. Phys. Chem. Chem. Phys. **2011**, 13, 6597-6609.

(9) Rubinstein, A.; Sabirianov, R. F.; Mei, W. N.; Namavar, F.; Khoynezhad, A. Effect of the ordered interfacial water layer in protein complex formation: a non-local electrostatic approach. Phys. Rev. E. **2010**, 82, 021915.

(10) Vogler, E.A. Water and the acute biological response to surfaces. Adv. Colloid Interface Sci. **1998**,74, 69-117.
(11) Worch, H. Special thin organic coatings. In: Metals as Biomaterials. Helsen, J.A. and Breme H.J., eds. Chichester: John Wiley & Sons, **1998**, 177-196.
(12) Juffer, A.H.; Argos, P.; de Vlieg, J. Adsorption of proteins onto charged surfaces: A Monte Carlo approach with explicit ions. J Comput. Chem. **1996**, 17(16),1783-1803.
(13) Kubiak-Ossowska, K.; Mulheran, P. A.; What governs protein adsorption and immobilization at a charged solid surface ? Langmuir **2010**, 26(11), 7690-7694.
(14) Tosaka, R.; Yamamoto, H.; Ohdomari, I.; Watanabe, T. Adsorption mechanism of ribosomal protein L2 onto a silica surface: a molecular dynamics simulation study. Langmuir **2010**, 26(12), 9950-9955.
(15) Sousa, S.R.; Manuela Bra´s, M.; Moradas-Ferreira, P.; Barbosa, M. A. Dynamics of fibronectin adsorption on TiO2 surfaces. Langmuir **2007**, 23, 7046-7054.
(16) Esposito, M.; Lausmaa, J.; Hirsch, J.M.; Thomsen, P. Surface analysis of failed oral titanium implants. J. Biomed. Mater. Res. **1999**, 48(4), 559-568.
(17) Namavar, F.; Cheung, C.L.; Sabirianov, R.F.; Mei, W.N.; Zeng, X.C.; Wang, G.; Haider, H.; Garvin, K. L. Lotus effect in engineered zirconia. Nano Lett. **2008**, 8, 988-996.
(18) Fukushima, K.; Yamada, I. Electrical properties of TiO2 films deposited by a reactive-ionized cluster beam. J. Appl. Phys. **1989**, 65, 619-623.
(19) Mayer, J.T.; Diebold, U.; Madey, T.E.; Garfunkel, E. Titanium and reduced titania overlayers on titanium dioxide (110). J. Electron Spectros. Related Phenomena **1995**, 73, 1-11
(20) Scopelliti, P.E.; Borgonovo, A; Indrieri, M; Giorgetti, L; Bongiorno, G; The Effect of Surface Nanometre-Scale Morphology on Protein Adsorption. PLoS ONE **2010** 5(7): e11862. doi:10.1371/journal.pone.0011862
(21) Meadows, P. Y.; Bemis, J. E.; and Walker, G, C. Single-Molecule Force Spectroscopy of Isolated and Aggregated Fibronectin Proteins on Negatively Charged Surfaces in Aqueous Liquids. Langmuir **2003**, 19, 9566-9572
(22) Bergkvist, M.; Carlsson, J.; Oscarsson S.J. Surface-dependent conformations of human plasma fibronectin adsorbed to silica, mica, and hydrophobic surfaces, studied with use of Atomic Force Microscopy. Biomed. Mater. Res. **2003,** 64A, 349-356.
(23) Baugh, L.;Vogel, V. Structural changes of fibronectin adsorbed to model surfaces probed by fluorescence resonance energy transfer. J. Biomed. Mater. Res. **2004**, 69, 525-534.
(24) Namavar, F.; Rubinstein, A.; Sabirianov, R. F.; Thiele, J G. M.; Sharp, G.; Pokharel, U.; Namavar, R. M.; Garvin, K. L. Engineered Nanostructured Coatings for Enhanced Protein Adhesion and Cell Growth. MRS Proceedings **2012,** 1418 .
(25) Rubinstein, A.; Sabirianov, R.; Namavar, F. Enhanced cell growth by nanoengineering zirconia to stimulate electrostatic fibronectin activation. Nanotechnology **2014**, 25, 065101.
(26) Singh, P.; Carraher, C.; Schwarzbauer, J.E. Assembly of Fibronectin Extracellular Matrix. Annu. Rev. Cell Dev. Biol. **2010**, 26, 397-419..
(27) Pan, H.; Qin, M.; Meng, W.; Cao, Y.; Wang, W. How do proteins unfold upon adsorption on nanoparticle surfaces? Langmuir **2012**, 28(35), 12779-12787.
(28) Ballet, T.; Boulange, L.; Brechet, Y.; Bruckert, F.; Weidenhaupt, M. Protein conformational changes induced by adsorption onto material surfaces: an important issue for biomedical applications of material science. Bull. Polish. Acad. Sc.: Tech. Sc. **2010,** 58(2), 30-315.

(29) Asthagiri, D.; Lenhoff, A.M. Influence of structural details in modeling electrostatically driven protein adsorption. Langmuir **1997**, 13, 6761-6768.
(30) Elcock, A.H.; Sept, D.; McCammon, J.A. Computer simulation of protein-protein interactions. Phys. Chem. B **2001**, 105, 1504-1518.
(31) Gilson, M.K.; Rashin, A.; Fine, R.; Honig, B. On the calculation of electrostatic interactions in proteins. J. Mol. Biol. **1985**,183, 503-516.
(32) Rubinstein,A.; Sherman,S. Influence of solvent structure on the electrostatic interactions in proteins. Biophys. J. **2004**, 87, 1544-1557.
(33) Pal, S.K.; Peon, J.; Bagchi, B.; Zewail, A.H. Biological water**:** femtosecond **dynamics of** macromolecular hydration**.** J. Phys. Chem. B **2002**, 106, 12376-12395.
(34) Pal, S.K.; Zewail, A.H. Dynamics of water in biological recognition. Chem. Rev. **2004**, 104, 2099-2123.
(35) Higo, J. ; Sasal, M.; Shirai, H.; Nakamura, H.;Kugimiya, T. Large vortex-like structure of dipole field in computer models of liquid water and dipole-bridge between biomolecules. Proc. Natl. Acad. Sci. USA **2001**, 9, 5961-5964.
(36) Massi, F.;Straub, J.E. Structural and dynamical analysis of the hydration of the Alzheimer's β-amyloid peptide. J. Comput. Chem. **2003**, 24, 143-153.
(37) Pal, S. K.; Peon, J.; Bagchi, B.; Zewail, A. H. Biological water: femtosecond dynamics of macromolecular hydration. J. Phys. Chem. B **2002**, 106, 12376.
(38) Pal, S. K.; Peon, J.; Zewail. A. H. Biological water at the protein surface: dynamical solvation probed directly with femtosecond resolution. Proc. Natl. Acad. Sci. U.S.A. **2002**, 99, 1763-1768.
(39) Pal, S. K.; Zewail, A. H.. Dynamics of Water in Biological Recognition. Chem. Rev. **2004**,104, 2099-2123.
(40) Rubinstein, A.; Sherman,S. Evaluation of influence of the internal aqueous solvent structure on electrostatic interactions at the protein-solvent interface by non-local electrostatic approach. Biopolymers **2007**, 87, 149-164.
(41) Kornyshev, A. A.; Vorotyntsev, M. A. Nonlocal electrostatic approach to the double layer and interface. Surf. Sci. **1980**, 101, 23-48.
(42) Jackson, J.D. Classical Electrodynamics, John Wiley & Sons: NY, **1998**.
(43) Rubinshtein, A.I. Image forces at the metal electrode-electrolyte solution interface: account of spatial dispersion of the solution permittivity. Phys. Stat. Sol. (b), **1983**, 20, 65-76.
(44) Misra, V. K.; Hecht, J. L.; Yang, A. S.; Honig, B. Electrostatic contributions to the binding free energy of the lambda cI repressor to DNA. Biophys. J. **1998**, 75, 2262-2273.
(45) Gray, P. R. ; Hurst, P. J.; Lewis, S. H.; Meyer, R. G. Analysis and Design of Analog Integrated Circuits (Fifth ed.). New York: Wiley. **2009**, p. 40.
(46) Ezhilvalavan, S.; Tseng, T.-Y. Electrical properties of Ta2O5 thin films deposited on Ta. J. Am. Ceram. Soc. **1999**, 82 (3), 600.
(47) Joshi, P.C.; Cole, M.W. Influence of postdeposition annealing on the enhanced structural and electrical properties of amorphous and crystalline Ta2O5 thin films for dynamic random access memory applications. J. Appl. Phys. **1999**, 86 (2), 871-880.
(48) Randall Jr., J. J.; Bernard, W. J.; Wilkinson, R. R. A radiotracer study of the composition and properties of anodic oxide films on tantalum and niobium. Electrochim. Acta **1965**, 10, 183-201.
(49) Harrop, P.J.; Wanklyn, J.N. The dielectric constant of zirconia.Br. J. Appl. Phys. **1967**, 18, 739-742

(50) Perry, N. H.; Kim, S.;Mason, T. O. Local Electrical and Dielectric Properties of Nanocrystalline Yttria-Stabilized Zirconia. J. Mater. Sci. **2008**, 43, 4684-4692.
(51) Roberts, S. Dielectric Constants and Polarizabilities of Ions in Simple Crystals and Barium Titanate. Phys. Rev. **1949**,**76**, 1215
(52) Frederikse, H. P. R. Permittivity (Dielectric Constant) of Inorganic Solids: CRC Handbook of Chemistry and Physics, CRC Press, Boca Raton, FL **2008**.
(53) Parker, R.A.; Wasilik, J.H. Dielectric constant and dielectric loss of TiO2 (rutile) at low frequencies. Phys. Rev. **1960**, 120, 1631-1637.
(54) Kornyshev, A. A.; Rubinshtein, A.I. Vorotyntsev, M. A. Model non-local electrostatics: I. J. Phys. C: Solid State Phys. **1978**, 11, 3307-3322.
(55) Kornyshev, A.A. Nonlocal screening of ions in a structurized polar liquid—new aspects of solvent description in electrolyte theory. Electrochim. Acta **1981**, 26, 1-20.
(56) Kornyshev, A.A.; Sutman, G.J. The shape of nonlocal dielectric function of polar liquids and the implications for thermodynamic properties of electrolytes. Chem. Phys. **1996**, 104, 1524-1544.
(57) Kornyshev, A.A.; Ulstrup, J. Polar solvent structural parameters from protonation equilibria of aliphatic and alicyclic diamines and from absorption bands of mixed-valence transition-metal complexes. Chem. Phys. Lett. **1986**, 126, 74-80.
(58) Kornyshev, A.A. Nonlocal electrostatics of solvations. In The Chemical Physics of Solvation, Part A. Edited by Dogonadze, R. R., Kalman, E., Kornyshev, A. A. and Ulstrup, J., Elsevier: Amsterdam. **1985**, 77–118.
(59) Obolensky, O. I.; Doerr, T.P.; Ray, R.;Yu, Y.-K. Rigorous treatment of electrostatics for spatially varying dielectrics based on energy minimization. Phys. Rev. E **2009**, 79, 041907.
(60) Bardhan, J. P. Nonlocal continuum electrostatic theory predicts surprisingly small energetic penalties for charge burial in proteins. J. Chem. Phys. **2011**, 135, 104113.
(61) Bardhan, J. P. Biomolecular electrostatics – I want your salvation (model). Comput. Sci. Disc. **2012**, 5, 013001.
(62) Dolatshahi-Pirouz, A.; Jensen, T.; Kraft, D.C.; Foss, M.; Kingshott, P.; Hansen, J.L.; Larsen, A.N.; Chevallier, J.; Besenbache, F. Fibronectin adsorption, cell adhesion, and proliferation on nanostructured tantalum surfaces. ACS Nano **2010**, 4, 2874-2882.
(63) MacDonalda, D.E.; Deo, N.; Markovic, B.; Stranick, M.; Somasundaran, P. Adsorption and dissolution behavior of human plasma fibronectin on thermally and chemically modified titanium dioxide particles. Biomaterials 2002, 23, 1269-1279.
(64) Scotchford, C.A. ; Ball, M.; Winkelmann, M.; Vörös, J.; Csucs, C.; Brunette, D.M.; Danuser, G.; Textor, M. Chemically patterned, metal-oxide-based surfaces produced by photolithographic techniques for studying protein- and cell-interactions. II: Protein adsorption and early cell interactions. Biomaterials **2003**, 24, 1147-1158.

Figure captions.

Figure 1. The charge Q located at the point (0, Z_0) of the cylindrical coordinate system, Z_0 is the distance to the interface.

Figure 2. The numerical calculation of the electrostatic energy of the unbound states ΔG^C for the charge located in the dielectric media (ceramic) as a function of the media dielectric constant for NL (Red) and CL (Blue) solvent consideration. Parameters of the solvent for the curves: (Blue) $\varepsilon_S = \varepsilon^* = 78.3$; (Red) $\varepsilon^* = 6$, $\varepsilon_s = 78.3$, L = 5 Å.The values of the dielectric constants of the ceramic materials are: polyethylene: $\varepsilon_C = 2$; quartz: $\varepsilon_C = 4$; ZrO_2: $\varepsilon_C = 25$; Ta_2O_5: $\varepsilon_C = \sim 30$; TiO2: $\varepsilon_C = 114$ (rutile). Calculations were performed with Z_0=2.5Å.

Figure 3. The electrostatic free energy ΔG_{EL} of the model protein-ceramic binding for non-local $\Delta G_{NL,EI}$ (Red) and classical $\Delta G_{CL,EI}$ (Blue) solvent consideration in depending on ceramic material dielectric constant ε_C. Calculations were performed with Z_0=2.5Å.

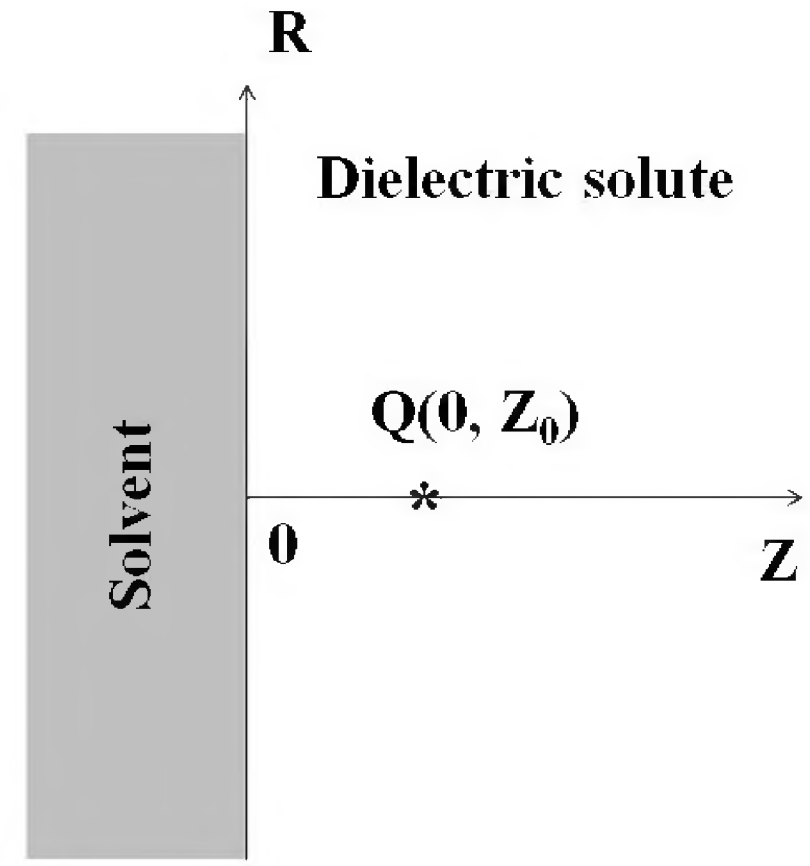

Figure 1

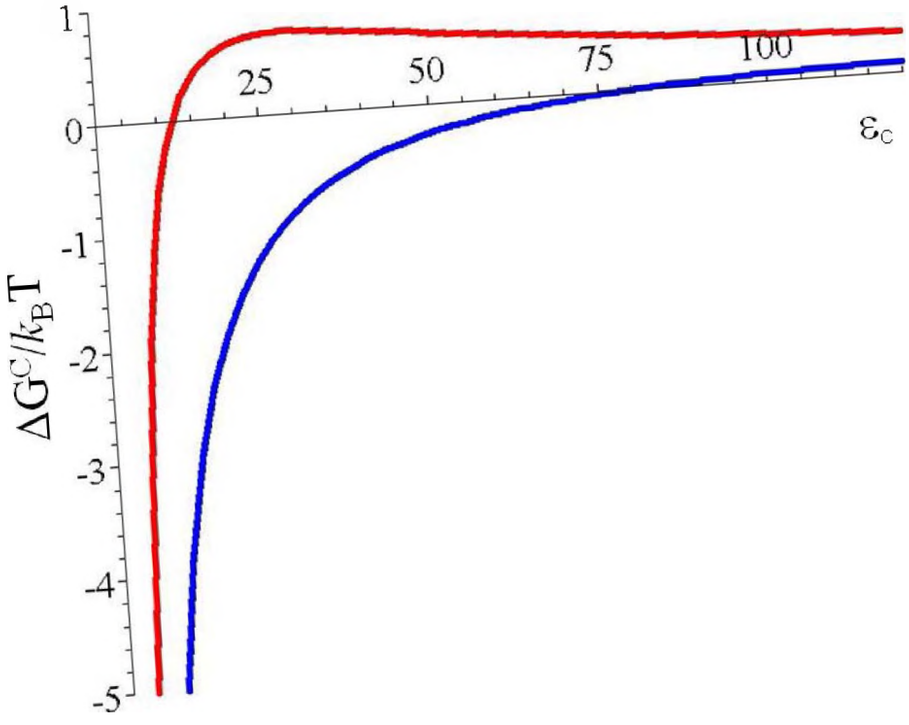

Figure 2.

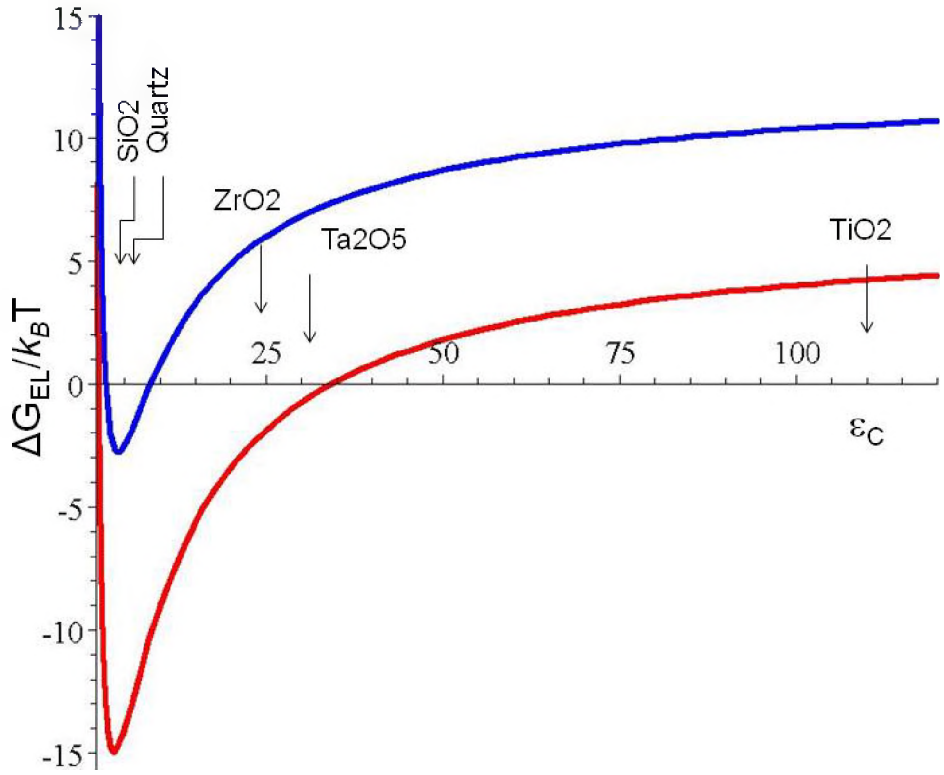
15
10
5
0
-5
-10
-15
SiO2
Quartz
ZrO2
Ta2O5
TiO2
25
50
75
100
$\Delta G_{EL}/k_BT$
ε_C

Figure 3

[1] Gray, J. The interaction of proteins with solid surfaces. Curr. Opin. Struct. Biol. **2004**, 14, 110-115.
[2] Wilson, K.; Stuart, S.J.; Garcia, A.; Lator Jr., R.A. A molecular modeling study of the effect of surface chemistry on the adsorption of a fibronectin fragment spanning the 7-10th type III repeats. J. Biomed. Mater. Res. **2004,** 69A, 686.
[3] Makrodimitris, K.; Masica, D. L.; Kim, E. T.; Gray, J. J. Structure prediction of protein-solid surface interactions reveals a molecular recognition motif of statherin for hydroxyapatite. J. Am. Chem. Soc. **2007**, 129, 13713-13722.
[4] Allen, L.T.; Tosetto, M.; Miller, I.S.; O'Connor, D.P.; Penney, S.C.; Lynch, I.; Keenan, A.K.; Pennington, S.R.; Dawson, K.A.; Gallagher, W.M. Surface-induced changes in protein adsorption and implications for cellular phenotypic responses to surface interaction. Biomaterials **2006**, 27, 3096-3108.
[5] Cutler, S.M.; Garcia, A.J. Engineering cell adhesive surfaces that direct integrin alpha5beta1 binding using a recombinant fragment of fibronectin. Biomaterials **2003**, 24,1759-1770
[6] Kasemo, B. Biological surface science. Surface Science **2002**, 500, 656-677.
[7] Hook, F.; Kasemo, B.; Grunze, M.; Zauscher, S. Quantitative Biological Surface Science: Challenges and Recent Advances. NANO **2008**, 12, 2428-2436.
[8] Sabirianov, R.F.; Rubinstein. A.; Namavar, F. Enhanced initial protein adsorption on engineered nanostructured cubic zirconia. Phys. Chem. Chem. Phys. **2011**, 13, 6597-6609.
[9] Rubinstein, A.; Sabirianov, R. F.; Mei, W. N.; Namavar, F.; Khoynezhad, A. Effect of the ordered interfacial water layer in protein complex formation: a non-local electrostatic approach. Phys. Rev. E. **2010**, 82, 021915.
[10] Vogler, E.A. Water and the acute biological response to surfaces. Adv. Colloid Interface Sci. **1998**,74, 69-117.
[11] Worch, H. Special thin organic coatings. In: Metals as Biomaterials. Helsen, J.A. and Breme H.J., eds. Chichester: John Wiley & Sons, **1998**, 177-196.
[12] Juffer, A.H.; Argos, P.; de Vlieg, J. Adsorption of proteins onto charged surfaces: A Monte Carlo approach with explicit ions. J Comput. Chem. **1996**, 17(16),1783-1803.
[13] Kubiak-Ossowska, K.; Mulheran, P. A.; What governs protein adsorption and immobilization at a charged solid surface ? Langmuir **2010**, 26(11), 7690-7694.
[14] Tosaka, R.; Yamamoto, H.; Ohdomari, I.; Watanabe, T. Adsorption mechanism of ribosomal protein L2 onto a silica surface: a molecular dynamics simulation study. Langmuir **2010**, 26(12), 9950-9955.
[15] Sousa, S.R.; Manuela Bra´s, M.; Moradas-Ferreira, P.; Barbosa, M. A. Dynamics of fibronectin adsorption on TiO2 surfaces. Langmuir **2007**, 23, 7046-7054.
[16] Esposito, M.; Lausmaa, J.; Hirsch, J.M.; Thomsen, P. Surface analysis of failed oral titanium implants. J. Biomed. Mater. Res. **1999**, 48(4), 559-568.
[17] Namavar, F.; Cheung, C.L.; Sabirianov, R.F.; Mei, W.N.; Zeng, X.C.; Wang, G.; Haider, H.; Garvin, K. L. Lotus effect in engineered zirconia. Nano Lett. **2008**, 8, 988-996.
[18] Fukushima, K.; Yamada, I. Electrical properties of TiO2 films deposited by a reactive-ionized cluster beam. J. Appl. Phys. **1989**, 65, 619-623.
[19] Mayer, J.T.; Diebold, U.; Madey, T.E.; Garfunkel, E. Titanium and reduced titania overlayers on titanium dioxide (110). J. Electron Spectros. Related Phenomena **1995**, 73, 1-11

[20] Scopelliti, P.E.; Borgonovo, A; Indrieri, M; Giorgetti, L; Bongiorno, G; The Effect of Surface Nanometre-Scale Morphology on Protein Adsorption. PLoS ONE **2010** 5(7): e11862. doi:10.1371/journal.pone.0011862

[21] Meadows, P. Y.; Bemis, J. E.; and Walker, G, C. Single-Molecule Force Spectroscopy of Isolated and Aggregated Fibronectin Proteins on Negatively Charged Surfaces in Aqueous Liquids Langmuir **2003**, 19, 9566-9572

[22] Bergkvist, M.; Carlsson, J.; Oscarsson S.J. Surface-dependent conformations of human plasma fibronectin adsorbed to silica, mica, and hydrophobic surfaces, studied with use of Atomic Force Microscopy. Biomed. Mater. Res. **2003,** 64A, 349-356.

[23] Baugh, L.;Vogel, V. Structural changes of fibronectin adsorbed to model surfaces probed by fluorescence resonance energy transfer. J. Biomed. Mater. Res. **2004**, 69, 525-534.

[24] Namavar, F.; Rubinstein, A.; Sabirianov, R. F.; Thiele, J G. M.; Sharp, G.; Pokharel, U.; Namavar, R. M.; Garvin, K. L. Engineered Nanostructured Coatings for Enhanced Protein Adhesion and Cell Growth. MRS Proceedings **2012,** 1418 .

[25] Rubinstein, A.; Sabirianov, R.; Namavar, F. Enhanced cell growth by nanoengineering zirconia to stimulate electrostatic fibronectin activation. Nanotechnology **2014**, 25, 065101.

[26] Singh, P.; Carraher, C.; Schwarzbauer, J.E. Assembly of Fibronectin Extracellular Matrix. Annu. Rev. Cell Dev. Biol. **2010**, 26, 397-419..

[27] Pan, H.; Qin, M.; Meng, W.; Cao, Y.; Wang, W. How do proteins unfold upon adsorption on nanoparticle surfaces? Langmuir **2012**, 28(35), 12779-12787.

[28] Ballet, T.; Boulange, L.; Brechet, Y.; Bruckert, F.; Weidenhaupt, M. Protein conformational changes induced by adsorption onto material surfaces: an important issue for biomedical applications of material science. Bull. Polish. Acad. Sc.: Tech. Sc. **2010,** 58(2), 30-315.

[29] Asthagiri, D.; Lenhoff, A.M. Influence of structural details in modeling electrostatically driven protein adsorption. Langmuir **1997**, 13, 6761-6768.

[30] Elcock, A.H.; Sept, D.; McCammon, J.A. Computer simulation of protein-protein interactions. Phys. Chem. B **2001**, 105, 1504-1518.

[31] Gilson, M.K.; Rashin, A.; Fine, R.; Honig, B. On the calculation of electrostatic interactions in proteins. J. Mol. Biol. **1985**,183, 503-516.

[32] Rubinstein,A.; Sherman,S. Influence of solvent structure on the electrostatic interactions in proteins. Biophys. J. **2004**, 87, 1544-1557.

[33] Pal, S.K.; Peon, J.; Bagchi, B.; Zewail, A.H. **Biological water**: **femtosecond** dynamics of **macromolecular hydration**. J. Phys. Chem. B **2002**, 106, 12376-12395.

[34] Pal, S.K.; Zewail, A.H. Dynamics of water in biological recognition. Chem. Rev. **2004**, 104, 2099-2123.

[35] Higo, J. ; Sasal, M.; Shirai, H.; Nakamura, H.;Kugimiya, T. Large vortex-like structure of dipole field in computer models of liquid water and dipole-bridge between biomolecules. Proc. Natl. Acad. Sci. USA **2001**, 9, 5961-5964.

[36] Massi, F.;Straub, J.E. Structural and dynamical analysis of the hydration of the Alzheimer's β-amyloid peptide. J. Comput. Chem. **2003**, 24, 143-153.

[37] Pal, S. K.; Peon, J.; Bagchi, B.; Zewail, A. H. Biological water: femtosecond dynamics of macromolecular hydration. J. Phys. Chem. B **2002**, 106, 12376.

[38] Pal, S. K.; Peon, J.; Zewail. A. H. Biological water at the protein surface: dynamical solvation probed directly with femtosecond resolution. Proc. Natl. Acad. Sci. U.S.A. **2002**, 99, 1763-1768.

[39] Pal, S. K.; Zewail, A. H.. Dynamics of Water in Biological Recognition. Chem. Rev. **2004**,104, 2099-2123.
[40] Rubinstein, A.; Sherman,S. Evaluation of influence of the internal aqueous solvent structure on electrostatic interactions at the protein-solvent interface by non-local electrostatic approach. Biopolymers **2007**, 87, 149-164.
[41] Kornyshev, A. A.; Vorotyntsev, M. A. Nonlocal electrostatic approach to the double layer and interface. Surf. Sci. **1980**, 101, 23-48.
[42] Jackson, J.D. Classical Electrodynamics, John Wiley & Sons: NY, **1998**.
[43] Rubinshtein, A.I. Image forces at the metal electrode-electrolyte solution interface: account of spatial dispersion of the solution permittivity. Phys. Stat. Sol. (b), **1983**, 20, 65-76.
[44] Misra, V. K.; Hecht, J. L.; Yang, A. S.; Honig, B. Electrostatic contributions to the binding free energy of the lambda cI repressor to DNA. Biophys. J. **1998**, 75, 2262-2273.
[45] Gray, P. R. ; Hurst, P. J.; Lewis, S. H.; Meyer, R. G. Analysis and Design of Analog Integrated Circuits (Fifth ed.). New York: Wiley. **2009**, p. 40.
[46] Ezhilvalavan, S.; Tseng, T.-Y. Electrical properties of Ta2O5 thin films deposited on Ta. J. Am. Ceram. Soc. **1999**, 82 (3), 600.
[47] Joshi, P.C.; Cole, M.W. Influence of postdeposition annealing on the enhanced structural and electrical properties of amorphous and crystalline Ta2O5 thin films for dynamic random access memory applications. J. Appl. Phys. **1999**, 86 (2), 871-880.
[48] Randall Jr., J. J.; Bernard, W. J.; Wilkinson, R. R. A radiotracer study of the composition and properties of anodic oxide films on tantalum and niobium. Electrochim. Acta **1965**, 10, 183-201.
[49] Harrop, P.J.; Wanklyn, J.N. The dielectric constant of zirconia.Br. J. Appl. Phys. **1967**, 18, 739-742
[50] Perry, N. H.; Kim, S.;Mason, T. O. Local Electrical and Dielectric Properties of Nanocrystalline Yttria-Stabilized Zirconia. J. Mater. Sci. **2008**, 43, 4684-4692.
[51] Roberts, S. Dielectric Constants and Polarizabilities of Ions in Simple Crystals and Barium Titanate. Phys. Rev. **1949**,**76**, 1215
[52] Frederikse, H. P. R. Permittivity (Dielectric Constant) of Inorganic Solids: CRC Handbook of Chemistry and Physics, CRC Press, Boca Raton, FL **2008**.
[53]Parker, R.A.; Wasilik, J.H. Dielectric constant and dielectric loss of TiO2 (rutile) at low frequencies. Phys. Rev. **1960**, 120, 1631-1637.
[54] Kornyshev, A. A.; Rubinshtein, A.I. Vorotyntsev, M. A. Model non-local electrostatics: I. J. Phys. C: Solid State Phys. **1978**, 11, 3307-3322.
[55] Kornyshev, A.A. Nonlocal screening of ions in a structurized polar liquid—new aspects of solvent description in electrolyte theory. Electrochim. Acta **1981**, 26, 1-20.
[56] Kornyshev, A.A.; Sutman, G.J. The shape of nonlocal dielectric function of polar liquids and the implications for thermodynamic properties of electrolytes. Chem. Phys. **1996**, 104, 1524-1544.
[57] Kornyshev, A.A.; Ulstrup, J. Polar solvent structural parameters from protonation equilibria of aliphatic and alicyclic diamines and from absorption bands of mixed-valence transition-metal complexes. Chem. Phys. Lett. **1986**, 126, 74-80.
[58] Kornyshev, A.A. Nonlocal electrostatics of solvations. In The Chemical Physics of Solvation, Part A. Edited by Dogonadze, R. R., Kalman, E., Kornyshev, A. A. and Ulstrup, J., Elsevier: Amsterdam. **1985**, 77–118.

[59] Obolensky, O. I.; Doerr, T.P.; Ray, R.;Yu, Y.-K. Rigorous treatment of electrostatics for spatially varying dielectrics based on energy minimization. Phys. Rev. E **2009**, 79, 041907.
[60] Bardhan, J. P. Nonlocal continuum electrostatic theory predicts surprisingly small energetic penalties for charge burial in proteins. J. Chem. Phys. **2011**, 135, 104113.
[61] Bardhan, J. P. Biomolecular electrostatics – I want your salvation (model). Comput. Sci. Disc. **2012**, 5, 013001.
[62] Dolatshahi-Pirouz, A.; Jensen, T.; Kraft, D.C.; Foss, M.; Kingshott, P.; Hansen, J.L.; Larsen, A.N.; Chevallier, J.; Besenbache, F. Fibronectin adsorption, cell adhesion, and proliferation on nanostructured tantalum surfaces. ACS Nano **2010**, 4, 2874-2882.
[63] MacDonalda, D.E.; Deo, N.; Markovic, B.; Stranick, M.; Somasundaran, P. Adsorption and dissolution behavior of human plasma fibronectin on thermally and chemically modified titanium dioxide particles. Biomaterials **2002**, 23, 1269-1279.
[64] Scotchford, C.A. ; Ball, M.; Winkelmann, M.; Vörös, J.; Csucs, C.; Brunette, D.M.; Danuser, G.; Textor, M. Chemically patterned, metal-oxide-based surfaces produced by photolithographic techniques for studying protein- and cell-interactions. II: Protein adsorption and early cell interactions. Biomaterials **2003**, 24, 1147-1158.

ResearchGate

See discussions, stats, and author profiles for this publication at: https://www.researchgate.net/publication/271797015

Comparing Biocompatibility of Nanocrystalline Titanium and Titanium-Oxide with Microcrystalline Titanium

Article *in* MRS Online Proceeding Library Archive · January 2013

DOI: 10.1557/opl.2013.804

CITATION
1

READS
22

8 authors, including:



Raheleh Miralami
University of Nebraska Medical Center
4 PUBLICATIONS **3** CITATIONS
SEE PROFILE



Laura Koepsell
Archer Daniels Midland Company
3 PUBLICATIONS **64** CITATIONS
SEE PROFILE



Geoffrey M Thiele
University of Nebraska Medical Center
192 PUBLICATIONS **3,409** CITATIONS
SEE PROFILE



Fereydoon Namavar
University of Nebraska Medical Center
254 PUBLICATIONS **2,386** CITATIONS
SEE PROFILE

All in-text references underlined in blue are linked to publications on ResearchGate, letting you access and read them immediately.

Available from: Raheleh Miralami
Retrieved on: 19 August 2016

Mater. Res. Soc. Symp. Proc. Vol. 1569 © 2013 Materials Research Society
DOI: 10.1557/opl.2013.804

Comparing Biocompatibility of Nanocrystalline Titanium and Titanium-Oxide with Microcrystalline Titanium

Raheleh Miralami[1], Laura Koepsell[1], Thyagaseely Premaraj[2], Bongok Kim[3], Geoffrey M. Thiele[4], J. Graham Sharp[5], Kevin L. Garvin[1], Fereydoon Namavar*[1]
[1]Department of Orthopaedic Surgery and Rehabilitation, UNMC, Omaha, NE
[2]Department of Growth & Development -, University of Nebraska-Lincoln, Lincoln, NE
[3]Department of Adult Restorative Dentistry, University of Nebraska - Lincoln, Lincoln, NE
[4]Department of Internal Medicine – Rheumatology, UNMC, Omaha, NE
[5]Department of Genetics, Cell Biology & Anatomy, UNMC, Omaha, NE
*Corresponding Author fnamavar@unmc.edu

ABSTRACT

Titanium (Ti) is the material of choice for orthopaedic applications because it is biocompatible and encourages osteoblast ingrowth. It was shown that the biocompatibility of Ti metal is due to the presence of a thin native sub-stoichiometric titanium oxide layer which enhances the adsorption of mediating proteins on the surface [1]. The present studies were devised to evaluate the adhesion, survival, and growth of cells on the surface of new engineered nano-crystal films of titanium and titanium oxides and compare them with orthopaedic-grade titanium with microcrystals. The engineered nano-crystal films with hydrophilic properties are produced by employing an ion beam assisted deposition (IBAD) technique. IBAD combines physical vapor deposition with concurrent ion beam bombardment in a high vacuum environment to produce films (with 3 to 70 nm grain size) with superior properties. These films are "stitched" to the artificial orthopaedic implant materials with characteristics that affect the wettability and mechanical properties of the coatings.

To characterize the biocompatibility of these nano-engineered surfaces, we have studied osteoblast function including cell adhesion, growth, and differentiation on different nanostructured samples. Cell responses to surfaces were examined using SAOS-2 osteoblast-like cells. We also studied a correlation between the surface nanostructures and the cell growth by characterizing the SAOS-2 cells with immunofluorescence and measuring the amount alizarin red concentration produced after 7 and 14 days. The number of adherent cells was determined by means of nuclei quantification on the nanocrystalline Ti, TiO_2, and microcrystalline Ti and analysis was performed with Image J. Our experimental results indicated that nanocrystalline TiO_2 is superior to both nano and microcrystalline Ti in supporting growth, adhesion, and proliferation. Improving the quality of surface oxide, i.e. fabricating stoichiometric oxides as well as nanoengineering the surface topology, is crucial for increasing the biocompatibility of Ti implant materials.

INTRODUCTION

Osseointegration of orthopaedic implants is dependent upon different parameters of the implant surface such as surface properties and physicochemical properties including surface energy, charge, wettability, chemistry, and topography. Surface topography can impact cellular behavior including adhesion, migration, morphology, and orientation in addition to focal adhesion, the development of cytoskeleton, and differentiation [2]. Surface modifications on implant surfaces can be manipulated by etching [3], plasma deposition [4], sintering powders [5], machining/micromachining [6], and ion-beam assisted deposition [7].

When an implant is placed in the body, a multi-step process occurs. First, serum/plasma proteins adsorb on the implant surface and cells attach to the protein layer by integrins which recognize presented extracellular ligands and mediate the initial interactions of cells and the implant material [8]. After the cells adhere, there is a rearrangement of cytoskeleton proteins, formation of tight focal adhesion contacts, activation of focal adhesion kinase, and the induction of several intracellular signal transduction pathways, which leads to proliferation and differentiation of the cells [8, 9]. Jager et al. and Stevens et al. have shown that roughened titanium surfaces can increase the focal contacts for cellular adhesion and they are able to guide membrane receptor organization and cytoskeletal assembly [10, 11]. In vitro experiments have shown that rough implant surfaces promote the adsorption of fibronectin and albumin [12, 13]. In vivo osteointegration has also been improved on roughened surfaces compared to smoother surfaces, which may suggest that the surface modulates the bone response including osteoblast differentiation, ECM deposition, and calcification [14, 15]. Hence, if there is an improvement in the symbiosis of the implant and osteointegration, it should accelerate the healing time, increase the implant longevity, and reduce the necessity of revision surgery [8].

In the present work, osteoblast function including cell adhesion, growth, and differentiation on different nanosamples were investigated. Cell responses to surfaces were examined using SAOS-2 osteoblast-like cells. We studied a correlation between the surface topography and the cell growth by characterizing the SAOS-2 cells with immunofluorescence and measuring the alizarin red concentration produced after 7 and 14 days.

MATERIALS AND METHODS

Sample Preparation The scientific community has been actively pursuing the study of IBAD for specific applications such as tribological coatings, anticorrosion coatings, optical coatings, superconducting buffer layers, and coatings for temperature sensitive substrates such as polymer. IBAD (Figure 1) combines evaporation with concurrent ion beam bombardment in a high vacuum environment. Energetic ions (with a depth penetration of typically less than 20 nm) were employed to produce engineered nanocrystals "stitched" to a substrate (utilizing billions and billions of directed and parallel ionic hammers). Ion bombardment is also the crucial factor for controlling other film properties such as surface morphology, density, stress level, crystallinity, grain size, grain orientation, and chemical composition [7].

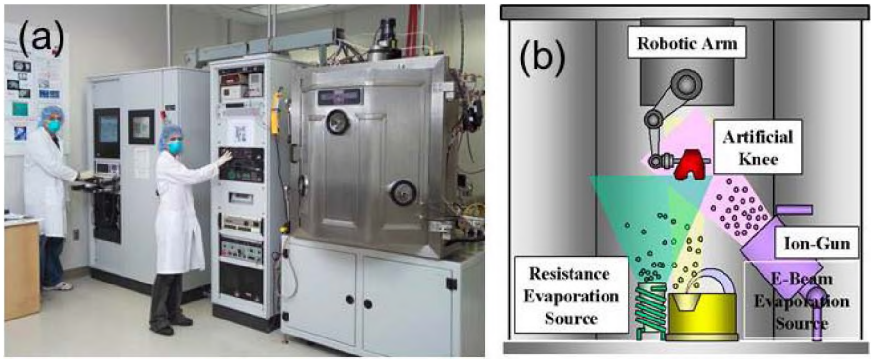

Figure 1. (a) IBAD system and (b) schematic. The process combines physical vapor deposition with concurrent ion beam bombardment to produce a wide range of nanocrystalline and coating [7].

The nanocrystalline TiO_2 and Ti samples were prepared by ion beam assisted deposition at the Nanotechnology Laboratory of the University of Nebraska Medical Center (Figure 1). The IBAD system is composed of a Veeco 12 cm RF ion gun that supplies ions at energies up to 1500 eV with a total current density of 500 mA, which provides a broad uniform ion beam of

oxygen, nitrogen, and argon. IBAD experiments were carried out in an ultrahigh vacuum environment at a base pressure of 10^{-8} Torr. Using this ion beam technique, we can easily create a gradual transition between the substrate material and the deposited film with less built-in stress than other techniques. These properties result in films with a much more durable adhesion to the substrate, even at room temperature. Ion bombardment also aids the production of stress-free films, eliminating stress-induced problems such as buckling, microcracking, or peeling. IBAD samples were cut into 1 cm^2 sections and placed in a 50:50 mixture of acetone: methanol. Samples were sonicated for 1 hour at room temperature, rinsed in ethanol, and dried under N_2 air. Samples were wrapped in foil and autoclaved before use.

Cell Culture and Cell Seeding

A human osteoblast-like cell line (SAOS-2) was used in this research. SAOS-2 cells were purchased from ATCC. Cells were grown in McCoy's 5A medium (ATCC) supplemented with 15% fetal bovine serum (FBS) and 1% gentamycin (Invitrogen) in a humidified 5% CO2 atmosphere at 37° C. Cells were seeded at a cell density of 10,000, 25,000, 50,000, and 75,000 cells/ml/cm^2 for cell adhesion and cell growth.

For differentiation experiments, cells were incubated in the standard McCoy's medium (supplemented with FBS and antibiotics) for 4 days. On day 4, 0.3 mM ascorbic acid and 10 mM glycerol phosphate were added to the medium (differentiating medium). The medium was changed every 3rd day and the cells were incubated for 7 and 14 days (mineralization).

Cell Adhesion and Fluorescence Imaging

The number of adherent cells was determined by means of nuclei quantification on the TiO_2-nano, Ti-nano, and Ti-micro substrates. Therefore, after 48 hours of incubation, SAOS-2 cells were washed gently with PBS. Then the cells were fixed with 4% formaldehyde for 10 minutes and stained with 300 nM DAPI (6-diamidino-2-phenylindole) for 5 minutes and rinsed. From each sample, 10 digital images were randomly taken with a Nikon camera using a planar 10x/0.25 objective. DAPI-stained nuclei were automatically counted after single-channel image segmentation and binary masking. The analysis was performed with Image J (Rasband, W.S., Image J, U. S. NIH, Bethesda, Maryland, USA, http://imagej.nih.gov/ij/, 1997-2012).

The morphology of focal adhesions and actin of SAOS-2 cells cultured on the samples were characterized by microscopy after immunofluorescent staining of actin (5:200, Invitrogen, CA, USA Alexa Fluor 546 Phalloidin) and DAPI (300 nM, Invitrogen, CA, USA 6-diamidino-2-phenylindole). Briefly, samples were gently rinsed in PBS and fixed with 4% formaldehyde for 10 minutes at room temperature. After another rinse in 1% PBS-bovine serum albumin (BSA; Sigma), cells were permeabilized with 0.1% Triton-X 100 solution in PBS. Samples were washed with PBS 3 times for 5 minutes at room temperature. Actin stain was added to each sample at a dilution of 5:200 for 30 minutes and rinsed with PBS 3 times for 5 minutes at room temperature. DAPI was added to each sample (300 nM) for 5 minutes and washed with PBS 3 times for 5 minutes at room temperature. Samples were mounted to slides and cover-slipped until further examination.

Alizarin red staining and quantification

Alizarin red staining was used in order to determine the calcium deposition of SAOS-2 osteosarcoma cells incubated on the nanosamples at day 7 and 14 using the Millipore Ostegenesis Assay Kit (ECM815) according to the manufacturer. Briefly, media was removed from the samples and rinsed with PBS. The nanosamples were fixed in 10% formaldehyde and stained with alizarin red stain for 20 minutes. The nanosamples were placed in 10% acetic acid for 30 minutes to remove the monolayer, placed in a microcentrifuge tube, and heated to 85°C

for 10 minutes and centrifuged. The supernatant was neutralized with 150 µl of 10% ammonium hydroxide and the absorbance was read at 405 nm.

Statistical Analysis All data presented were derived from three independent experiments (n=3) and within one experiment three separate samples were analyzed. The results are presented as mean ± SD. Statistical significant differences between three different substrates for alizarin red experiments were evaluated using ANOVA with post-hoc Bonferroni's multiple comparison tests.

RESULTS

Morphology of IBAD nanocrystalline Ti and TiO_2 determined by atomic force microscopy (AFM) and is shown in Figure 2.

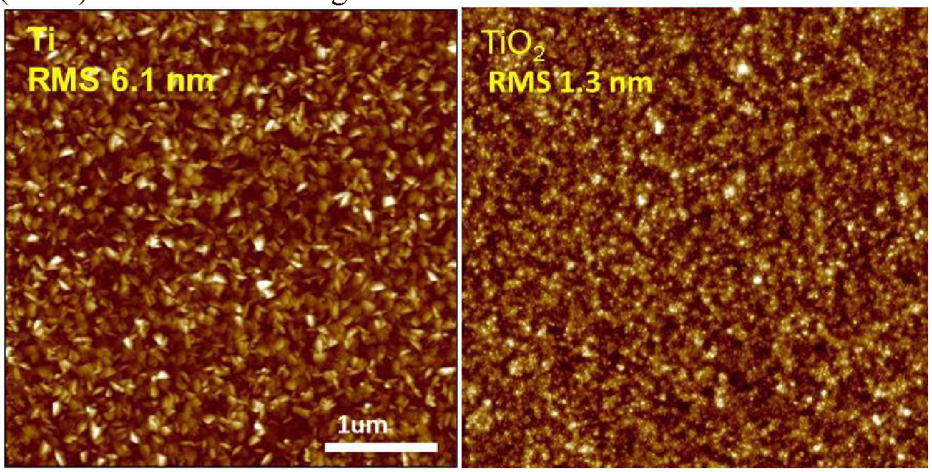

Figure 2. AFM images (5µm scan size) of ion beam deposited nano crystalline Ti and TiO_2 deposited at room temperature (a) Ti with a RMS of 6.1 nm (b) TiO_2 with a RMS of 1.3 nm.

Cell Adhesion SAOS-2 cells were monitored for adhesion to the nanocrystalline TiO_2, Ti, and medical grade of Ti substrates at 48 hours. The number of adherent cells was determined by nuclei quantification with DAPI in Figure 3. Figure 3a shows a higher number of nuclei on nanostructured surfaces compared to biomedical grade Ti, which indicates more adhesion and growth on nano surfaces. However, by only observing DAPI stained cells, it is impossible to know if cells are healthy and prolific on the surface or not; besides DAPI staining, we also monitored actin fiber shapes (Figure 3b and 3c) that show a significant difference in cell shape on nano crystalline TiO_2 and Ti as compared to micro crystalline Ti.

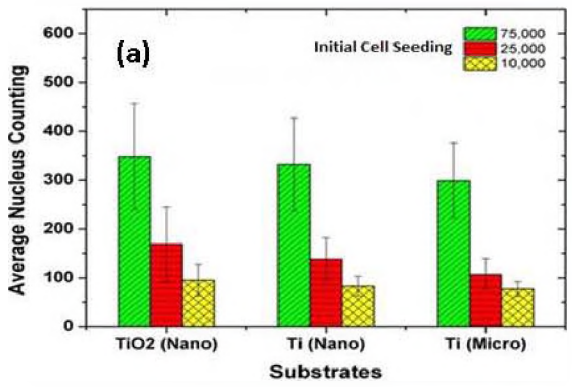

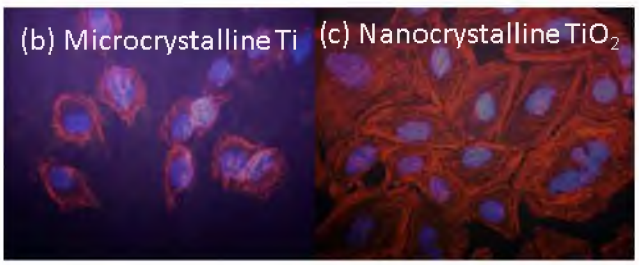

Figure 3. (a) Comparing the number of nuclei of SAOS-2 cells on different substrates using DAPI at 48 hours, (b) and (c) merged actin and DAPI stained cells on microcrystalline Ti and nanocrystalline TiO_2, respectively.

Cell Morphology

In order to evaluate the morphology of cells adherent to the various substrates, the attached cells were labeled with actin and DAPI. Pronounced, large focal adhesions or thin, round shapes with actin staining indicate larger surfaces available for adhesion and thus stronger adhesion contacts between cell and material [16]. From Figure 2, the overall cell morphology is flattened, cells are well spread on the substrate, and the used timing (48 hours of incubation) allowed the cell to go through one cell cycle, which is also an indicator of the suitability of the substrate.

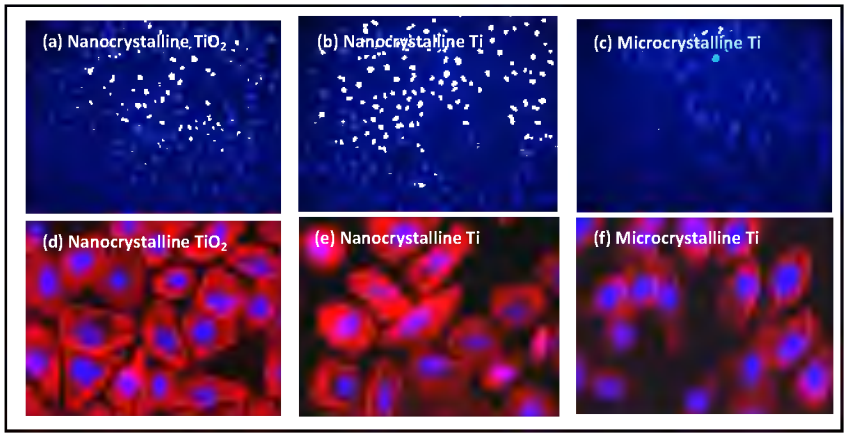

Figure 4. Comparing cell adhesion on nanocrystalline TiO_2, Ti, and biomedical grade of Ti by fluorescence images microscopy. 50000 cells were incubated for 48 hours. (a), (b) and (c) are DAPI and (d), (e) and (f) are actin stain experiments.

Alizarin Red Quantification

In order to determine the calcium deposition of SAOS-2 on osteosarcoma cells incubated on different substrates on the 7th day and 14th day of the culture, alizarin red staining was performed. Alizarin Red-S Staining (ARS) is a dye that binds selective calcium salts and is ideally used for calcium mineral histochemistry [17]. Results of a typical experiment performed in quadruplicate are shown. Values are given as means ± SD.

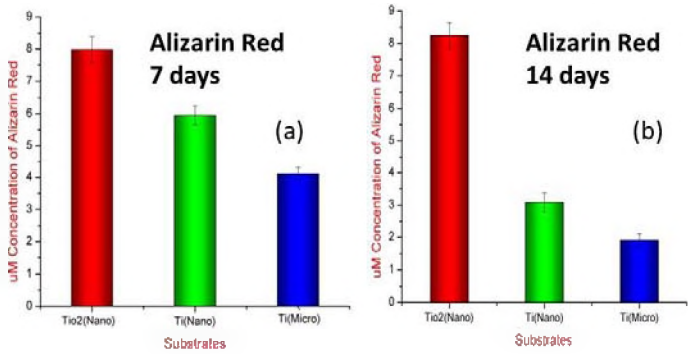

Figure 5. Comparing calcium deposition on different substrates using Alizarin Red Assay which indicates that more calcium deposited on IBAD nanocrystalline TiO_2 and Ti as compared to biomedical Ti.

CONCLUSIONS

Fluorescence images presented in Figure 4 show that cell body shape is dependent on the surface of the substrate. If the cell appears round, it is possible that the cells recognize the surface as "flat" and unstructured. However, the nanoroughness of the nano-substrate surfaces appears comparable in size and structure, causing the cells to attach only slightly and to search for suitable places for optimal anchoring [18]. Figure 5 shows the observed matrix mineralization

(Calcium) in SAOS-2 cells. Osteoblastic cells deposit calcium in order to support bone construction. The cells cultured on the nanosurfaces clearly show bright orange-red staining which implies a higher degree of differentiation of the cells. Therefore, enhanced bone formation ability can be expected from the developed nanostructured surfaces. Our statistical analysis indicates that calcium deposition on nano-crystalline TiO_2 is significantly different from biomedical grade of Ti after 7 days. These results indicate that the surface nanostructures affect cell interactions at the surface and alter cell behavior when compared to conventional (microstructures) size topography.

Nanostructured surfaces possess unique properties that alter cell adhesion by direct (cell–surface interactions) and indirect (affecting protein–surface interactions) mechanisms [18]. Indeed, in recent work we have shown that the nano-engineered cubic zirconia is superior in supporting growth, adhesion, and proliferation as compared to the microstructured one [19]. Since cell attachment is mediated by adhesive proteins such as fibronectin (FN), we performed a comparative analysis of adsorption energies of FN fragment using quantum mechanical calculations and Monte Carlo (MC) simulation, both on smooth and nanostructured surfaces. We have found that an FN fragment adsorbs significantly more strongly on the nanostructured surface than on the smooth surface [20].

Acknowledgment:
This work was supported by DOE grant (DE-SC0005318), Material Science Smart Coating.

References

1. F. Namavar, R. Sabirianov, et al, presented at the 2012 Annual Meeting of the Orthopaedic Research Society, San Francisco, Feb 2012 (unpublished).
2. M. Lord, M. Foss, F. Besenbacher, Nano Today 5, 66-78 (2010).
3. T.J. Webster, C. Ergun, et al, J. Biomed. Mater. Res. A **67** (3), 975-80 (2003).
4. M. Svehla, P. Morberg, W. Bruce, B. Zicat, et al, J. Arthroplasty **17** (3), 304-11 (2002).
5. P.R. Klokkevold, P. Johnson, S. Dadgostari, et al, Clin. Oral. Implants. Res. **12**, (4), 350 (2001).
6. D.M. Brunette, B. Chehroudi, J. Biomech. Eng. **121** (1), 49-57(1999).
7. F. Namavar, C.L. Cheung, R.F. Sabirianov, et al, NanoLetters **8** (4) 988 (2008).
8. M. Kalbacova, B. Rezek, V. Baresova, et al, Acta Biomater. **5** (8) 3076-85 (2009).
9. J.B. Kim, P. Leucht, C.A. Luppen, et al, Bone **41** (1) 39-51 (2007).
10. M. Jager, et al, J. Biomed. Biotechnol. 8, 69036 (2007).
11. M.M. Stevens, J.H. George, Science **310** (5751) 1135-8 (2005).
12. L. Le Guehennec, M.A. Lopez-Heredia, B. Enkel, et al, Acta Biomater. **4** (3) 535-43 (2008).
13. P. Francois, P. Vaudaux, M. Taborelli, et al, Clin. Oral Implants Res. **8** (3) 217-25 (1997).
14. Y. Wu, J.P. Zitelli, K.S. TenHuisen, X. Yu, M.R. Libera, Biomaterials. **32** (4) 951-60 (2011).
15. B.D. Boyan, L.F. Boneweld, E.P. Paschalis, et al, Calcif. Tissue Int. **71** (6) 519-29 (2002).
16. O. Babchanko, A. Kromka, et al, Physica. Status Solidi A **206** (9) 2033-7 (2009).
17. H.T. Sasmazel, Int. J. Biol. Macromol. 49, 838–846 (2011).
18. G. Mendonca, D.B. Mendonca, F.J. Aragao, et al, Biomaterials **29** (28) 3822-3835 (2008).
19. F. Namavar, R.F. Sabirianov, et al in *Engineered Nanostructured Coatings for Enhanced Protein Adsorption and Cell Growth* (Mater. Res. Soc. Symp. Proc. **1418**, Boston, MA 2011).
20. R.F. Sabirianov, A. Rubinstein, F. Namavar, Phys. Chem. Chem. Phys. **13** (14) 6597 (2011).

Mater. Res. Soc. Symp. Proc. Vol. 1578 © 2013 Materials Research Society
DOI: 10.1557/opl.2013.880

Nanostructurally Designed Ultra-hydrophilic Hard Ceramic Oxide Coatings for Orthopaedic Application

Fereydoon Namavar*[1,7], Renat F. Sabirianov[2,7], Jiaming Zhang[3], Chin Li Cheung[4,7], Charles Blatchley[5], Raheleh Miralami[1], John G. Sharp[6], and Kevin L. Garvin[1]
[1]Department of Orthopaedic Surgery and Rehabilitation, UNMC, Omaha, NE
[2]Department of Physics, University of Nebraska at Omaha, Omaha, NE
[3]Department of Geological Sciences and Materials Science & Engineering, University of Michigan, Ann Arbor, MI
[4]Department of Chemistry University of Nebraska - Lincoln, Lincoln, NE
[5]Department of Physics, Pittsburg State University, Pittsburg, KS
[6]Department of Genetics, Cell Biology & Anatomy, UNMC, Omaha, NE
[7]Nebraska Center for Materials and Nanoscience, University of Nebraska - Lincoln, Lincoln, NE

ABSTRACT

This paper addresses the application of engineered nanocrystalline ultrahydrophilic titanium oxide films to artificial orthopaedic implants. Titanium (Ti) is the material of choice for orthopaedic applications and has been used for over fifty years because of its known bio-compatibility. Recently it was shown that biocompatibility of Ti metal is due to the presence of a thin native sub-stoichiometric titanium oxide layer [1] which enhances the adsorption of mediating proteins on the surface thus enhancing cell adhesion and growth [2,3,4]. Improving the quality of surface oxide, i.e. fabricating stoichiometric oxides as well as nanoengineering the surface topology that matches the dimensions of adhesive proteins, is crucial for the increase of protein adsorption [2] and, as a result, the biocompatibility of Ti implant materials. We have fabricated ultrahydrophilic nano-crystalline transparent films of anatase phase of titania (TiO_2) by ion beam assisted deposition (IBAD) processes in an ultrahigh vacuum system. Source material was 99.9% pure rutile TiO_2. Various ion beam conditions were used to produce these coatings with different grain sizes (4 to 70 nm) that affect the wettability, roughness, and the mechanical and optical properties of the coating [5]. Our biological experiments have shown that biocompatibility of these ultrahydrophilic nanoengineered TiO_2 coatings are superior to commonly used orthopaedic titanium and even hydroxyapatite.

INTRODUCTION

Total joint arthroplasty is a remarkably successful procedure to restore mobility in patients with reduced joint function due to disease or injury and typically exhibits a ten to fifteen-year lifespan. Artificial knee, hip, and shoulder implants rank 1, 2, and 3 in terms of the numbers of each joint replaced in the United States, respectively. According to the American Academy of Orthopaedic Surgeons reports [6], hip and knee replacements will number over four million annually by 2030. The rate of revision surgeries are projected to remain at about 18% and 8% of primary hip and knee replacements, respectively [6]. Enhancing biointegration will lead to rapid bone growth, faster patient recovery, and a substantial savings of healthcare dollars.

Orthopaedic and dental implants have used various coatings, such as hydroxyapatite, to encourage osseointegration. However, concerns have been raised about the mechanical strength, debonding, and bioabsorption of these layers [7-8]. We have designed and engineered novel, hard, mechanically and chemically stable, ultra-hydrophilic, nanocrystalline TiO_2 coatings to support bone ingrowth. We have demonstrated fabrication of thin film of amorphous, rutile [9],

brookite, and anatase [10] phases of TiO_2 by ion beam assisted deposition (IBAD) processes. Comparing the IBAD nanocrystalline transparent anatase TiO_2 films with the orthopaedic materials indicates that IBAD TiO_2 is superior in supporting growth, adhesion, and proliferation of the bone marrow stromal cell line.

EXPERIMENTS

Nanocrystalline TiO_2 is produced by ion beam assisted deposition in the Nanotechnology Laboratory at the University of Nebraska Medical Center [5]. IBAD experiments were carried out in an ultrahigh vacuum environment at a base pressure of 10^{-8} Torr. Energetic ions (oxygen, nitrogen, and argon) are employed to produce engineered nanocrystals "stitched" to a metallic substrate by ion bombardment using an "ionic hammer". We have applied IBAD to TiO_2 thin films deposited at room temperature to 600° C onto silicon (Si), glass, and orthopaedic-grade titanium substrates [5]. Because of space limitations, we briefly discuss the results for anatase TiO_2 in this work.

The thin film characteristic and surface morphology of IBAD TiO_2 films produced at different deposition conditions and their relationship to their hydrophilicity were studied by transmission microscopy (TEM), atomic force microscopy (AFM), and contact angle measurements. TEM studies on these films revealed that these films are composed of nanocrystallites. The average roughness and grain size of these films ranges from 3 to 70 nm as the deposition temperature increases from room temperature to 600° C. X-ray diffraction was applied to determine the crystal structures. The wetting characteristic of TiO_2 was observed by measuring the contact angle of a deionized (DI) water droplet on the surfaces of various samples using a computer-controlled video contact angle (VCA) instrument (Optima XE from AST Product, Inc, MA). The droplet was dispensed from an automated syringe with a consistent and controlled droplet size of 0.25 μL. The contact angle was then measured by fitting curves to the sample surface and drop geometry. Ten drops were analyzed on each test component with at least 3 test components for each material. The contact angle for each material was then determined by averaging the measurements obtained on different areas of the same sample. In addition to AFM and scanning electron microscopy (SEM), the surface roughness measurement was performed on a non-contact optical interferometer (Xi-100 by Ambios Technology, CA) which combines the phase-shifting interferometric technology with optical imaging to provide the roughness of the curve surfaces with high precision.

SAOS-2 human osteoblast-like cell line was used for the tests. Cells were grown in McCoy's 5A medium with 15% Fetal Bovine Serum and 1% gentamycin. Cells were plated on samples at different cell densities (25,000 and 50,000 cells/ml/cm^2) and 48 hours incubation time for cell adhesion experiments. Staining with DAPI (300 nM, Invitrogen, 6-diamidino-2-phenylindole), 10 random pictures were taken from each sample at 10x and adherent cells were counted using ImageJ software. Cell morphology was visualized by microscopy at 40x after staining with actin (5:200, Invitrogen, Alexa Fluor 546 Phalloidin) and DAPI.

RESULTS

The phase identification of the TiO_2 films was investigated by x-ray diffractometry (XRD) using a Bruker AXS D8 Discover with a GADDS area detector at 10 cm from the sample and with a conventional copper target x-ray tube set at 40 kV and 30 mA. The weighted average wavelength of the Cu Kα = 1.5417 Å. Figure 1a demonstrates a typical spectrum obtained for anatase TiO_2 [10]. The rutile and amorphous phases of nanocrystalline TiO_2 films were produced

by higher ion beam intensity (i.e. higher ions to atoms arrival ratio) as compared to those used for fabrication of the anatase phase. Deposition and characterization of the rutile and amorphous phases of TiO_2 are discussed and reported in reference [9]. It should be noted that formation of the anatase phase is independent of deposition temperatures; however, the grain size of TiO_2 increases from a few to 70 nm for increasing the temperature from room to 600° C, respectively. Atomic force microscopy (AFM) was employed to investigate the surface morphology of the as-deposited TiO_2 thin films (Figure 1b). It should also be noted that we have produced TiO_2 films with roughness ranging from 1 to 70 nm by varying IBAD conditions (ion species) [10]; however, higher roughness can be obtained at higher temperatures. Structural characteristics for a typical anatase TiO_2 film using an oxygen beam was determined by SEM and high resolution as demonstrated in Figure 2. Figure 3 shows two images of advancing contact angles selected out of 100 recorded frames (10 frames/s) for a TiO_2 film.

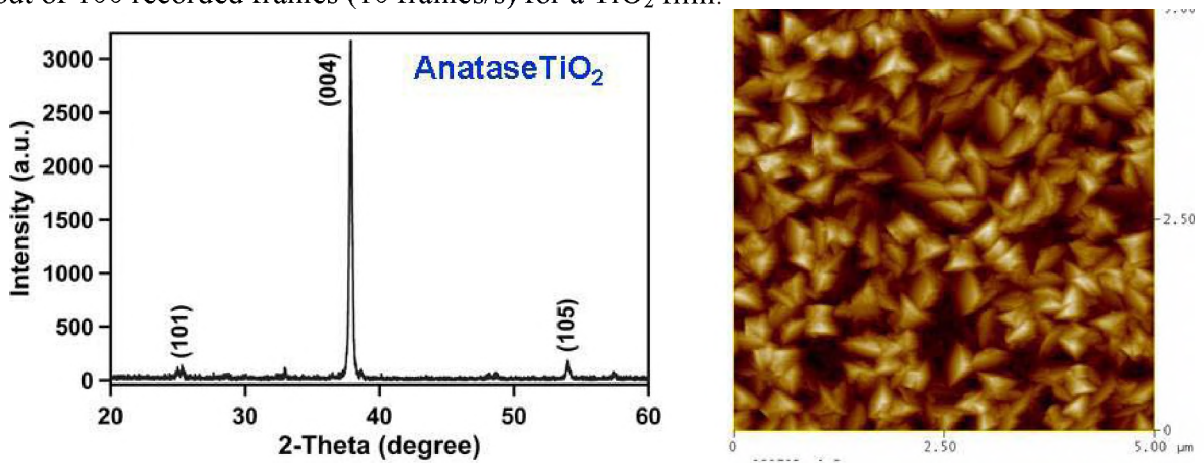

Figure 1. X-ray diffraction and AFM images (5µm scan size) of IBAD nanocrystalline TiO_2 onto a silicon substrate. AFM of TiO_2 shows a RMS of 70 nm for deposition at 600° C. Note that IBAD deposition without external heating produces a surface roughness of 5 to 15 nm, depending on IBAD conditions (ions species, nitrogen, oxygen, and argon beams).

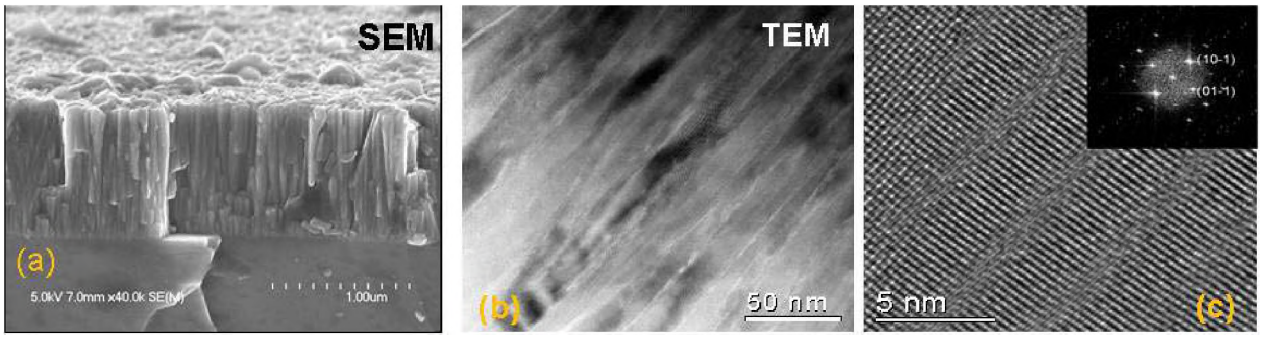

Figure 2. (a) SEM, (b) TEM, and (c) high-resolution transmission electron microscopy (HRTEM) images show the nanocrystalline anatase TiO_2 on Si substrate. Highly textured grains are grown from substrate to the surface, resulting in formation of extruding granular columns with dimension ~30 nm in width (also seen in TEM images (b)). HRTEM image with lattice fringes in (c) shows the symmetry of anatase crystal viewed along [111] (FFT in the inset).

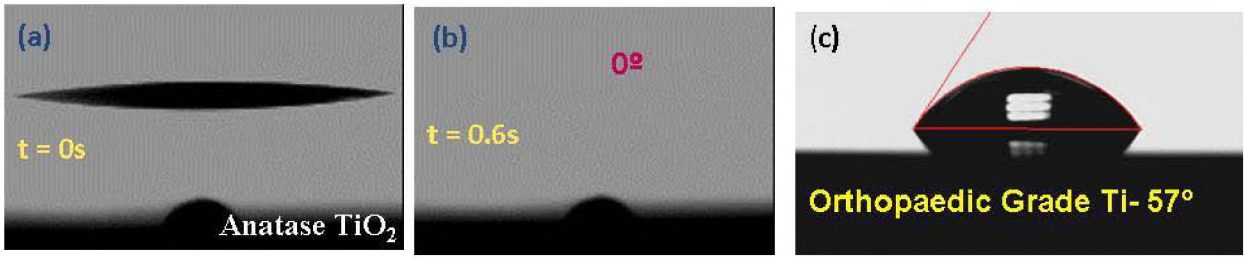

Figure 3. Video camera image of a contact angle of nanocrystalline anatase TiO_2 demonstrating the spreading of a 0.25 µL water droplet shows two images of advancing contact angles selected out of 100 recorded frames (10 frames/s) for a TiO_2. (a) After the droplet was brought in contact with the TiO_2 surface, time 0s. (b) After 0.6s contact angle became zero, i.e. complete wettability. (c) Contact angles measured of orthopaedic-grade Ti with micro crystal structure. Nanocrystalline TiO_2 films retained their hydrophilic properties for over a year during which they were under observation.

A zero contact angle can be observed after 0.06 s of droplet deposition. To explain the origin of wettability of our films, the surface morphology of TiO_2 samples was studied by AFM where the presence of semi-pyramidal nanostructures was observed. Ultrahydrophilic behavior of these films may be explained by the Wenzel model [11]. Figure 4 demonstrates cell numbers as determined by counting DAPI-stained nuclei, after 48 hours incubation. Data were derived from three independent experiments and within each experiment three separate samples were analyzed. Statistical significant differences between nano and micro substrates for different cell densities were evaluated using ANOVA with post-hoc Bonferroni's multiple comparison tests ($p=0.028$ for 25,000 and $p=0.035$ for 50,000 initial cell seeding numbers). The higher number of DAPI-stained nuclei on nano-TiO_2 compared to micro-Ti shows higher cell adhesion and growth on nanocrystalline surface of TiO_2.

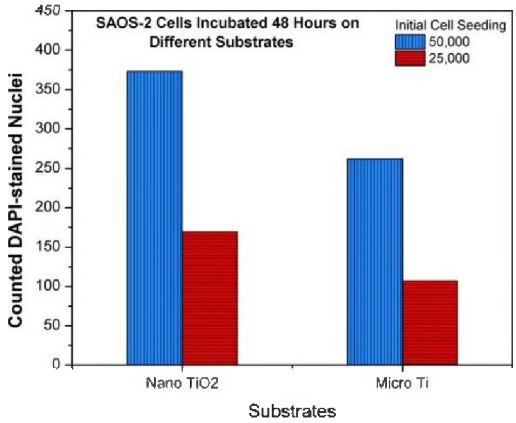

Figure 4. Demonstrates SAOS-2 cells adhesion and growth on nanocrystalline TiO_2 as compared with biomedical-grade of titanium. SAOS-2 cells were seeded with an initial number of 50,000 cells (blue) and 25,000 cells (red), respectively. The differences between adherent cells on TiO_2 and Ti, for both densities, were determined to be statistically significant.

Figure 5 also shows there are greater numbers of cells on nanocrystalline anatase TiO_2 compared to microcrystalline Ti. In addition, most of the adherent cells on the nanocrystalline TiO_2 are spread and the actin filaments are evident. Although there was variability in different areas of the biomedical-grade Ti, overall, fewer cells on the microcrystalline Ti are adhered and spread, some of cells are rounded up, and some have nucleus fragmentation indicating apoptosis and cell death. Overall, cell survival, adhesion, and morphology indicated that the cells growing on the nanocrystalline TiO_2 are healthier than those growing on biomedical grade Ti.

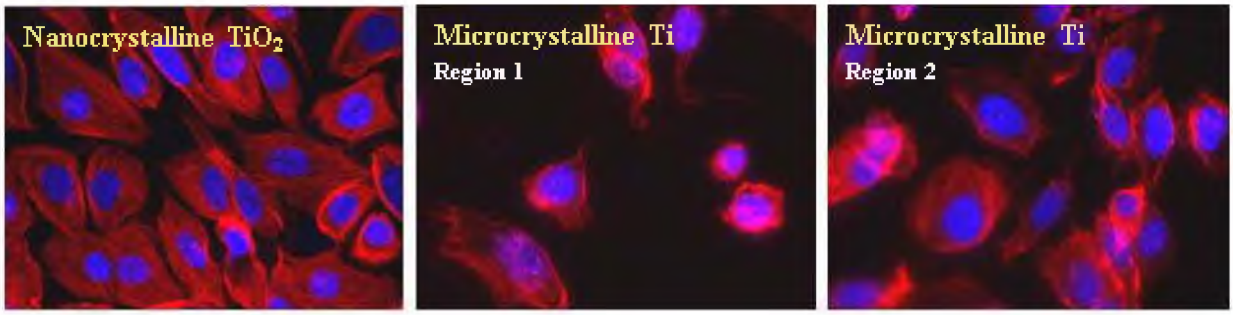

Figure 5. Comparing visualization of the morphology and adherence of SAOS-2 cells on nanocrystalline TiO_2 and biomedical-grade titanium by fluorescence microscopy at 400 X at the same growing conditions and 48 hours of incubation. Most of the adherent cells on the nanocrystalline TiO_2 are spread and actin filaments (red) are evident as compared to titanium, which some cells are rounded up and their nucleus (blue) are fragmented.

DISCUSSION

Titanium dioxide is a very unusual material. It becomes hydrophilic upon UV radiation and as-prepared films of TiO_2 show zero contact angle on smooth surfaces [12]. However, after a few days, the angle gets larger reaching even 90 degrees. Our as-deposited nanostructured coatings exhibit contact angle of 0 degrees. A few weeks later, contact value increases slightly. After one year one, our samples have shown contact angles of 14 degrees which is considerably lower than previously observed without UV light treatment. We explain this effect within Wenzel's model. The ratio between true and apparent surface area is called Wenzel's ratio [4, 11]. According to the Wenzel's model, the apparent contact angle, φ, on the rough surface is related to the Young's contact angle, θ, as $\cos(\varphi)=r\cos(\theta)$. If the contact angle of the flat surface is less than 90 degrees, which is frequently true for anatase TiO_2, then the apparent contact angle is smaller than the Young's contact angle. For example, if Wenzel's ratio r=2.5 and Young's contact angle $\theta=70^o$ then the apparent contact angle φ is equal to 31 degrees. We observe a similar effect in zirconia; however, the surface of zirconia has lower Young's contact angle of about 50 degrees. This makes wicking transition at smaller Wenzel's ratio. It is sufficient to have surface roughness r=1.55 to get complete spreading of the drop. AFM profile of TiO_2 fabricated by IBAD is observed by AFM to be very large, despite small rms roughness. This may explain increased wettability of nanostructured TiO_2. Beside Wenzel's mechanism, the nanostructured surface of titania has a large variation in symmetry and stoichiometry of surface termination. This facilitates the formation of a large number of sites possessing local electric polarization at the surface and enhances the wettability of TiO_2 as well as interaction with adhesive proteins.

Surface wettability and morphology affect the adhesion of cells to a surface. In cell-cell adhesion, one of the extracellular matrix (ECM) proteins, fibronectin (FN), mediates the interactions between cells by insoluble FN matrix. The FN absorption is considered in the literature as one of the most essential events in cell adhesion and bone formation on the implant surface [13]. Together with other adhesive proteins and proteins incorporated into ECM [13 14], FN dimer mediates the cell adhesion to the implant surface. Particularly, FN dimer plays the role of specific anchor and signal factor for cells on the implant surface and provides focal or cell–matrix adhesion. Thus, the FN adsorption is a key factor in cell adhesion and bone formation at an implant surface [14, 15]. Recently we have demonstrated that FN may adhere stronger to the nanostructured surface than to the planar smooth surface due to the roughness fitting to the size

of FN and its complementary electrostatically to the protein (due to the locally charged patches originated by nanostructuring) [2]. The adsorption of protein on nanocrystalline surface of implants is analogous to the formation of protein–protein complexes. In protein complex formation, both steric (shape fit) and electrostatic complementarity of the interacting proteins contributes to the lock-and-key specific recognition mechanism. (See reference 2 for details). In comparative ELISA experiments studying adsorption of FN onto the elemental Ti and IBAD nanocrystalline stoichiometric TiO_2, we observed [1] a significant increase of FN adsorption on TiO_2 versus Ti. Higher FN adsorption may facilitate faster cell adhesion to the surfaces and their proliferation. We have carried out a comparative animal studies [16] by using an intramedullary implant model and compared the undernourished old rats with younger rats. These results indicate that the maturation of the newly formed bone in the undernourished older rats with the nanoengineered coating is comparable to that in the younger rats with only Ti implants.

CONCLUSION

Our results indicate that nano-engineering TiO_2 coatings with grain sizes ranging from 2 to 10 nm, which is comparable with the dimension of adhesive protein, will enhance cell adhesion and growth. Nanocrystalline ceramics such as TiO_2 and ZrO_2 possess unique properties that alter cell adhesion by direct (cell–surface interactions) and indirect (affecting protein–surface interactions) mechanisms [2]. This result is consistent with our recent animal studies [16] that show faster and better quality bone growth on a titanium implant coated with the nanostructure ceramics.

ACKNOWLEDGMENT

This work was supported by DOE grant (DE-SC0005318), Material Science Smart Coating.

REFERENCES

1. F. Namavar, et al., Why is Titanium biocompatible? Orthopaedic Research Society Annual Meeting, San Francisco, CA, (2012).
2. R.F. Sabirianov, A. Rubinstein, F. Namavar, Phys. Chem. Chem. Phys. 13 (14), 6597 (2011).
3. F. Namavar; A. Rubinstein, et al., Mater. Res. Soc. Symp. Proc. 1418, 2012).
4. R. Miralami, et al. In press, Mater. Res. Soc. Symp. YY Spring Meeting (2013).
5. F. Namavar, C.L. Cheung, R.F. Sabirianov, et al., Nano Lett. 8 (4), 988-996 (2008).
6. S. Kurtz, et al., 73rd Annual Meeting of the AAOS, Chicago, IL, (2006).
7. A. El-Ghannam, Expert Rev. Med. Devices, 2 (1): 87-101; 1340-1347 (2005).
8 O. Reikeras, R.B.Gunderson, Acta Orthop Scand. 73 (1), 104-108 (2002).
9. J. Zhang, J. Lian, F. Namavar, et al., J Phys Chem C, 115 (46) 22755 (2011).
10. G.Wang, J.R. Brewer, F. Namavar, R.F. Sabirianov, Scanning 30, 59–64 (2008).
11. R. N. Wenzel, Ind. Eng. Chem, 28, 988 (1936).
12. R. Wang, K. Hashimoto, A. Fujishima, M. Chikuni, et al., Nature 388, 431 (1997).
13. A.G. Hemmersam, et al., J Colloid Interface Sci, 320,110-116 (2008).
14. C.S. Chen, et al., Biochem Biophys Res Commun 307, 355-361 (2003).
15. S.R. Sousa, et al., Lengmuir, 23, 7046-7054 (2007).
16. A. Dusad, D. Chakkalakal, F. Namavar, et al., Proc IMechE Part H: J Engineering in Medicine, 27 (5) 510-522 (2013).